



University of Crete, School of Sciences and  
Engineering, Department of Physics

**Dissertation:**

**Detecting hidden sketch drawings and fresco layers using a  
novel, photoacoustic, diagnostic approach**

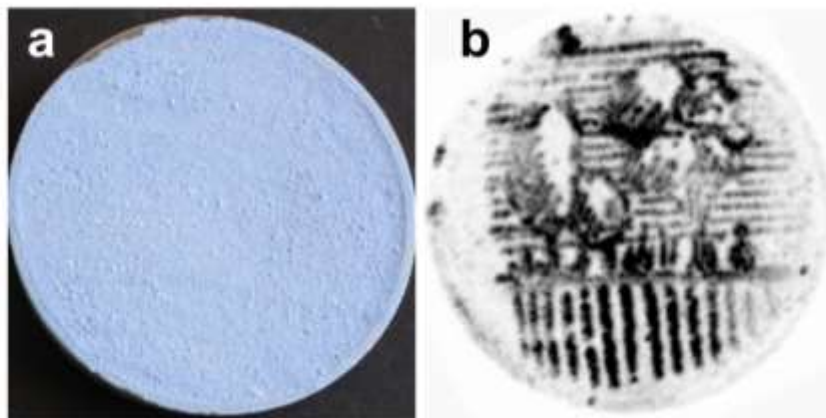


Figure 1: (a) Brightfield view of photoacoustic sample coated with acrylic paint. (b) Recovered pattern of the underlying sketch through photoacoustic imaging.

Evgenia Klironomou

Supervisor: Peter Rakitzis

Research Associate: George Tserevelakis

Heraklion, June 2021

## **Acknowledgements**

Foremost, I would like to sincerely thank my supervisor, Pr. Peter Rakitzis and Dr. Giannis Zacharakis, for giving me the chance to work and familiarize with the laboratory environment of an important research center such as FORTH.

My gratitude also goes to Dr. George Tserevelakis, who has been on my side during this long journey, giving me guidance, council and support while helping me overcome my fear of taking initiative while gaining experience during the realization of the experiments.

What is more, I would like to thank Ms. Kristalia Melessanaki for the preparation of the mock-ups that were used for the needs of this work and for the insight she provided me with, concerning the materials and methods used in mural painting.

In addition, I would like to thank Mr. Hatzigiannakis Kostas for photographing the samples with the MSI apparatus and also Dr. Panagiotis Siozos and Angelos Filippidis, for theirs hints and tips.

Finally, I would like to thank my friends and family for being there for me in times of struggle and pressure during this journey.

# Table of Contents

Acknowledgements .....	1
1. Introduction.....	4
1.1. The importance of underdrawings.....	4
1.2. Drawing materials and Grounds.....	4
1.2.1. Drawing materials .....	4
1.2.2. Grounds and carriers.....	6
1.3. Existing imaging techniques .....	7
1.3.1. Infrared Photography .....	7
1.3.2. Infrared Reflectography .....	9
1.3.3. Multispectral Infrared Reflectography.....	10
1.3.4. X-Ray Fluorescence .....	11
1.3.5. Optical Coherence Tomography.....	12
1.3.6. Terahertz Radiation.....	13
1.3.7. Limitations of existing techniques.....	15
2. Theoretical background – tools.....	15
2.1. General information.....	15
2.2. Ultrasound propagation .....	17
2.2.1. Acoustic waves .....	17
2.2.2. Reflection and transmission of acoustic waves.....	17
2.3. Derivation of the general photoacoustic equation .....	19
2.4. Photoacoustic equation under thermal confinement.....	20
2.5. Requirements of effective heat production.....	22
2.6. Spotsize and fluence calculation .....	23
2.7. Spatial resolution.....	23
2.8. The Nyquist-Shannon Theorem.....	24
2.9. Absorbance spectrums.....	24
3. Experimental setup .....	26
4. Methods .....	27
4.1. Sample preparation.....	27
4.2. Acquisition.....	28
4.3. Data analysis.....	28
5. Results .....	29
5.1. Chromium Samples .....	29
5.2. Various pigments.....	35

6. Discussion.....	39
7. Summary.....	41
8. References.....	42

## 1. Introduction

The aim of this work is to develop a novel, non-invasive, photoacoustic imaging (PAI) technique, which will be used for the detection and the imaging of hidden features, like underdrawings, of murals. The idea of detecting underdrawings in works of art has been intriguing for the majority of art conservators, as it is possible to elicit interesting information about an artwork. In PAI, a pulsed laser interacts with the sample, in order to locate and map the spatial distribution of absorbing components, by exploiting the ultrasonic acoustic waves that are being produced. During the past decade, a number of studies have taken place in the area of the conservation of cultural heritage with modern means, by taking advantage of the development of new technologies. In regard to artwork diagnostics, there are many bibliographical references that indicate the importance of such applications for the artistic community.

### 1.1. The importance of underdrawings

As an underdrawing we define the initial sketch or drawing made to plan the design of an illustration. An underdrawing can range from extremely detailed drawings to abstract sketches. During the time of their making, the artists could not imagine that underdrawings were going to present any interest, thus they are typically hidden beneath the paint layers in fully painted and finished works of art. However, if these hidden drawings are able to be visualized, they can provide a great deal of information about an artist's working process, by revealing how carefully a composition may have, or have not, been planned. What is more, they can provide evidence for the presence of more than one artistic hand, and document changes made between the design stage and the final stage of the creation, which is, of course, the painting. All this extra information presents a whole new world in front of the eyes of the conservators, as they can extract more details about the psychosynthesis or the mood of the painter, his methods and the way he proceeds during the formation of his creation. Additionally, the mapping of well-known paintings of popular artists, can dictate the working style of each artist, and this can be further used in order to prove the authenticity of newly discovered paintings, or in general, artworks whose authenticity could not be proved with traditional means.

### 1.2. Drawing materials and Grounds

#### 1.2.1. Drawing materials

**Graphite** is a crystalline form of carbon which is widely distributed naturally as a mineral in different parts of the world. Nowadays, the most important source is Sri Lanka; European sources have been Cumberland, Bavaria, and Bohemia, where deposits have been worked for centuries. Graphite can also be made artificially by a furnace process since about 1891. Graphite has long been used as a writing material and it gets its name appropriately from the Greek “γράφειν” (to write). It was early confused with lead which was also used for writing purposes, and hence the names ‘black lead’ and plumbago are also used for it. For use in lead pencils, it is compressed with very fine clay. Graphite has a greasy texture and is dull gray. Graphite is one of the most stable and refractory of materials and would be permanent in any technique. It has been used chiefly as a drawing material.

**Carbon Black** includes various pigments that are derived from the partial burning or carbonizing of natural gas, oil, wood, and other organic materials. Almost none of these products are pure carbon. Carbon makes a very stable pigment that it is unaffected by light and air, or by hot concentrated acids and alkalis. It can only be destroyed by burning at very high temperatures.

**Silver Point** has been the most common of the metal points used for drawing. In all of these the principle is the same. When the silver point is drawn over a properly coated ground (with very lean structure), fine particles of the metal are taken off and left in the line that has been described. It is a pale gray mark which in time corrodes slightly to a darker value and a warmer tone.

**Ink** is a liquid or viscous material used for writing, printing, lithographing, stamping, and staining. Inks are made from dyes and from pigment suspensions, like carbon black. Those used for printing and lithographing are made by grinding pigments in oils and varnishes. Ordinary writing inks are iron gall inks, in which the color and stain are formed by the combination of gallotannic acid (one of the two forms of tannic acid) from oak galls and green vitriol in the presence of air.

**Lamp Black** is nearly pure (over 99%), amorphous carbon which is collected in brick chambers from the condensed smoke of a luminous flame from burning mineral oil, tar, pitch, or resin. It is slightly bluish in color, and makes good neutral grays. Microscopically, it is very finely divided, uniform, and homogeneous; in mounting mediums, the particles appear to collect in chains and filaments. It does not wet well with water on account of the slight amount of unburned oil it contains.

**Chalk** is a natural deposit, a slaty, soft, earthy material and is very rich in carbon. It is widely used for drawing. As now prepared for the market, the various colors of drawing chalk are put up in small sticks or as pencils. Their use dates back to ancient times and they were as well very common during the Renaissance.

**Charcoal Black** is the residue from the dry distillation of woods and is made by heating the wood in closed chambers or kilns. When produced from smooth wood such as willow, bass, beech or maple it has the best quality. It may be used in stick form for sketching purposes and for the preparation of cartoons.

**Vine Black**, which is similar to charcoal, is prepared by carbonizing vine twigs or vine wood. Other similar vegetable blacks are made from peach stones, cocoon shells, cork, etc.

**Ivory Black** was made by charring chips of ivory, its use was established in antiquity by the example of Apelles, but there is no evidence that it was continued in the Middle Ages. The standard black pigments of medieval times may be taken as lampblack and charcoal, each from several sources, with lampblack from oil and charcoal from vine sprigs probably in the lead.

**Crayon** is a small stick for drawing, composed usually of pigment in an oil or wax. It is smooth and ordinarily used on paper. The use of crayons in Europe evidently began in Italy in the middle of the sixteenth century. Another type of crayon was made in the seventeenth century by dipping and cooking charcoal in linseed oil.

**Sinopia** (also known as sinoper, named after the now Turkish city Sinop) is a dark reddish-brown natural earth pigment, whose reddish color comes from hematite, a dehydrated form of iron oxide. It was widely used in Classical Antiquity and the Middle Ages for painting, and during the Renaissance it was often used on the rough initial layer of plaster for the underdrawing for a fresco. The word came to be used both for the pigment and for the preparatory drawing itself, which may be revealed when a fresco is stripped from its wall for transfer.

### 1.2.2. Grounds and carriers

The word “ground” in connection with paintings is a little ambiguous. For example, is a picture is painted on a brick wall covered with plaster, either the brick or the plaster might be called the ground. By common consent, however, nowadays, the plaster in this case is called the “ground”, and the brick wall the “carrier.” Thus, in a panel painting, the wooden panel is called the carrier, and the layer of gesso, or plaster, or whatever there may be between the wood and the painting, is called the ground. (Grounds on canvas are still usually called “primings”). Sometimes there is no distinction, and others, the carrier itself is also the ground. The latter appears most commonly in writings, drawings or paintings on paper or parchment.

**Canvas** is, literally, a coarse cloth made from cotton, hemp or flax. This definition serves well enough to describe the traditional fabric used as a paint support in Europe, though hemp fiber is rarely found in such objects. The word ‘canvas’ has now a number of meanings. It may be used for artists’ canvas or for a picture painted on canvas.

**Palimpsest** is a manuscript page, usually from parchment or paper, from which the original text has been scored and scratched to provide a good bond for the new, and the old surface ruthlessly covered and repainted. Sometimes the older members of these palimpsests have not been roughened, but simply plastered over, or even simply whitewashed, in preparation for the new decoration. Repainting of this sort has sometimes had the effect of preserving for us paintings or texts which might otherwise have been lost.

**Lime** is the standard medieval binding medium for wall painting. If a particle of pigment is surrounded by lime water, and the water dries away, the particle of pigment gets caught in the net of lime crystals. This binding effect may be accomplished by two methods. One is to mix lime water with the pigments; and the other is to mix the pigments with plain water only and apply them to fresh lime plaster. In this second case, the water with which the pigments are mixed mingles with the lime-saturated moisture of the fresh plaster, and the amount of lime mixed with the colors as a result is usually the minimum. There is no excess of lime to cloud or dull them, as there is apt to be when they are deliberately mixed with lime or lime water before they are applied. Furthermore, they dry with the plaster, as a part of it, and not as a surface layer, more or less detached from the wall itself, as in the first system.

Nevertheless, a great deal of medieval painting was done on walls which had previously dried. The wall was damped down with lime water and a little lime or lime water was mixed with each color as it was applied. There is abundant evidence that this was the dominant method of European wall painting in the Middle Ages. Its chief rival, were oil painting, in England and Northern Europe and, after the beginning of the fourteenth century, in Southern Europe, the process known as buon fresco (“true fresco”) painting.

**True Fresco** first appeared in the fourteenth century in Italy and it became a common practice to plaster walls in bits, and to paint on the fresh plaster with untempered colors, simply mixed with water, leaving the lime of the plastered wall to act as the binder for the pigments.

In true fresco, the artist draws his work full size on the rough plaster foundation, and covers only so much of it with fresh plaster as he hopes to be able to finish in a day. He undercuts the edge of each section as he finishes it, and interweaves the adjoining plaster neatly under the cut edge of previous days’ work. True fresco may be recognized by the division of the painted surface by these joints

between successive pieces of fresh plastering; but this is not binding, as many works called fresco will be found to have been executed by other means. For instance, joints of this sort appear in lime paintings which are not true fresco. They simply mean that parts of the painting were unsatisfactory, so that they were cut away, replastered, and painted over.

**Secco Painting:** To supplement the painting methods which depended on the binding action of lime, egg tempera was used on walls; but this method of painting involved hard work and was generally confined to developing an effect already partially established. Certain colors, especially blacks and blues, were dulled and dimmed by the whiteness of the crystallized lime binder, and they were usually applied with egg or size. Lime painting, whether on a dry wall or in fresco, did not lend itself readily to the deliberate execution of fine detail; and it was quite usual practice to depend on finishing with egg or size, until Renaissance times, when it became a popular “accomplishment”, and finally an obsession, to complete a painting entirely on the wet plaster without retouching a secco.

### **1.3. Existing imaging techniques**

As it was mentioned before, the detection of underdrawings is a matter of great importance and thus, many research teams have developed a number of techniques over the years. Each method has its advantages and its drawbacks and this is the reason why the detection of the underdrawings for a work of art usually happens in more than just one manner. It is also possible that different techniques provide the researchers with supplementary information. Below are presented the most popular techniques used for imaging in cultural heritage.

#### **1.3.1. Infrared Photography**

First discovered in 1910s infrared photography owes its existence to the American physicist Robert Williams Wood, who experimented with the infrared (IR) region of the electromagnetic spectrum. The irradiation of the specimen is done with lamps commonly used in photography, which produce light in the visible and IR spectrum. Part of the radiation is absorbed from the specimen while the rest is reflected and is recorded on a camera film with spectral range up to 900nm. With the use of the proper filter, the visible part cannot reach the camera lens, and hence, only the IR is collected. The use of this technique for paintings can also provide information about the potential existence of cracks in the upper layers of the pigment. Hence it is considered as an important tool for the preservation of paintings.

During the irradiation of the sample, a number of optical phenomena can be observed, such as light absorption or reflection and, of course, scattering. At the IR region the percentage of light that is being absorbed or scattered is relatively lower than the percentage of the visible spectrum. Thus, IR radiation can penetrate and reach deeper into the painting. During the transmission through the volume of the painting a percentage of the IR radiation is again reflected and absorbed, but a sufficient amount reaches the depth where the underdrawings lay. The materials used for the underdrawings (like charcoal or graphite) have high absorption coefficients in IR, unlike the pigments that lay above. Infrared Photography is a non-invasive, non-contact technique, as the painting is not touched during the procedure. What is more, the photos can provide information about the exact location of the underdrawings relatively to the visible area of the painting, as the image resembles to a superposition of the different layers of the painting. Nevertheless, this superposition can potentially confuse the observer, because he cannot distinguish from which depth originates every piece of information. Also, the areas underneath darker pigments (like dark green, blue, black etc.)

appear a lot darker, and thus the technique is efficient in colors like red, brown and white. Finally, the penetration of the IR radiation is related to the depth of the total paint layer. This is why it is not possible to acquire sufficient information from paintings with many layers of pigments with IR photography. The attenuation of the radiation in this case happens due to the scattering of the light during its transmission in the paint layers.

A beautiful example where the IR Photography was used is the painting “The Good Samaritan”, which has been attributed to a follower of the Dutch painter Jan van Scorel. The artwork was created



in 1537. It is interesting to mention the fact that after the detection of the underdrawings, the researchers mentioned that they could distinguish between the sketches these that had been drawn by the apprentice and the ones made by Scorel himself. These were used by the follower as guidelines in order to create his work of art. Most importantly though, the researchers brought to light certain features of this artist's working procedure.

Figure 2: “The Good Samaritan”.

The underdrawn figure of the wounded man has a narrower waist, tapering limbs, and hands and feet half the size of their painted counterparts. In other words, the proportions of the underdrawn figure are at first glance more closely related to Scorel.



Figure 3: IR Photography of a detail of the artwork. The lines and curves drawn by the apprentice are visible on every part of the body of the wounded Jew.

### 1.3.2. Infrared Reflectography

Infrared Reflectography (IRR) has been investigated since the 1960s, although the origins can be traced back to the 1930s, when IR photography was first proposed for the detection of underdrawings. The technique follows the same rules as IR Photography concerning the irradiation of the painting and the scattering, reflecting and absorbing phenomena that take place. In particular, the IR Reflectography, thanks to the properties of transparency of the pigments to the infrared radiation, allows the visualization of features underneath the surface of paintings, such as the underdrawing sketch, or subsequent repaintings. The main difference between the two techniques lies in the method of detection of the reflected light. In IRR, the collection of the reflected radiation occurs with a specific imaging system (that consists of optics and a camera) sensitive in the spectral region of approximately  $2\mu\text{m}$ .

The detection system converts IR radiation in visible and presents the result on a screen. The detection ability of the underdrawing, like in IR photography, is reduced while the depth of the paint layers is augmenting. What is more, the detection ability is inversely proportional to the absorbance coefficients of the paint layers. The advantage of IRR compared to IR Photography is that IRR has the means to provide information from other regions of the artwork, which are covered with blue or green pigments. It is important to underline the fact that the technological advancement of the IR detectors through the years has given the analogous enhancement at the results. Still though, the final image that is produced cannot separate the upper from the lower layers and thus it appears as a superposition of the sum of the paint layers and the underdrawings.



Figure 4: "Carrying of the Cross".

An interesting example of the IRR technique is Jan van Scorel's *"Carrying of the Cross"* (1530, oil on panel, 48.3 x 32.9 cm. Private collection, New York.). In Figure 4, a detail of the artwork is featuring the original and the IRR image respectively, where the hidden sketches are visible. The underdrawing on this work of art is loosely sketched in black chalk. It is not impossible that it was made by Scorel himself, but a shop assistant cannot be excluded.



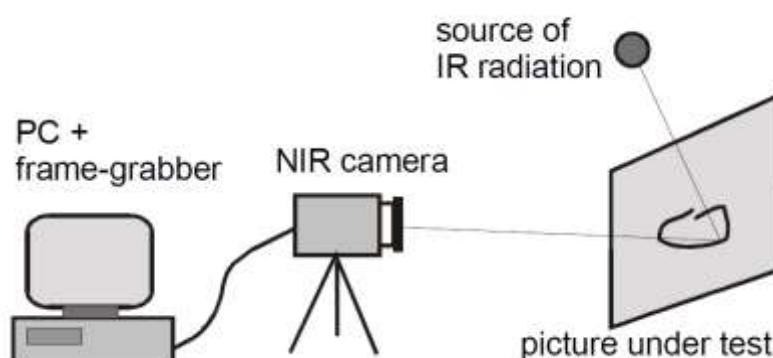
Figure 5: (a) Photo of the artwork. (b) IR Reflectogram of the same area presented in (a), where the underdrawing is visible.

Another popular artwork where IRR was applied is the “Virgin of the rocks” by Leonardo Da Vinci. There are two versions of this painting, one at the Louvre Museum and the other at the National Gallery of London.

### 1.3.3. Multispectral Infrared Reflectography

Multispectral Infrared Reflectography, also known as Multispectral Imaging (MSI) is a commonly used technique in the domain of underdrawings detection. It got to the forefront of the branch of Cultural Heritage at the beginning of 1990. It is obvious from its name that the technique is based on the foundations of IR Reflectography. The difference of the two methods lies in the readjustment of the Multispectral IR Reflectography into a technique which acquires multiple images in different, narrow spectral bands of the IR spectrum. It was first applied for qualitative comparison of the different bands, in order to identify areas of different material composition, natural degradation, past conservation intervention, preparatory sketches, and quantitatively for improved precision in color measurement. Later, with increased number of bands and speed of acquisition, it was used to extract spectral reflectance information for pigment identification. The spectral images that acquired in the different bands are stacked in a spectral cube where the x and y axes represent a point on the image and the z axis shows its reflectance over each spectral image. The final composition provides information that exceeds our knowledge due to IR Reflectography. The technique can be used for the analysis and authentication of pigments in paintings. MSI encounters the same limitation because of

the light scattering and reflection as IRR, and this is why the technique cannot be used in works of art with thick or numerous paint layers.



An example of the use of the MSI is a painting by Carlo Crivelli, “*Saint Mary Magdalene*” from the National Gallery of London (NG907.2).

Figure 6: Basic configuration of an IRR system.

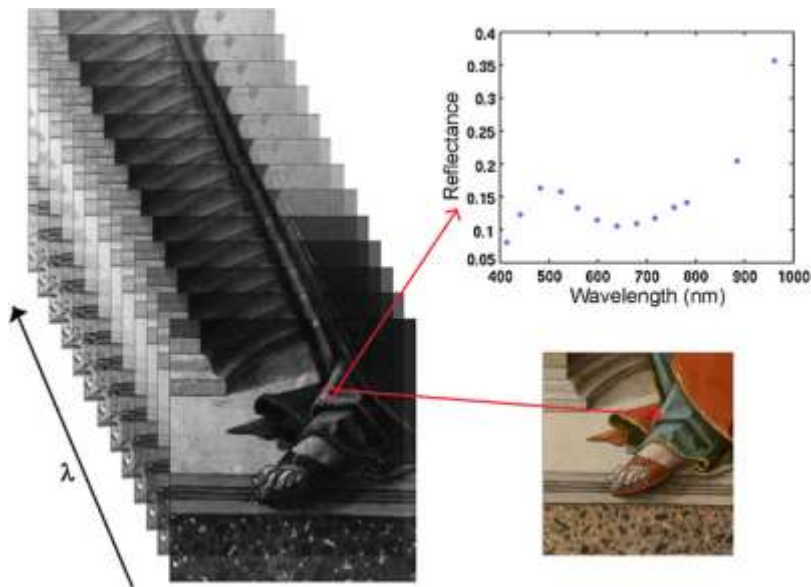


Figure 7: A schematic diagram illustrating a spectral cube obtained from multispectral imaging, the color image derived from the spectral cube and a spectrum for a point on the *blue color* which can be identified with the pigment “Azurite”.



Figure 8: “Saint Mary Magdalene”.

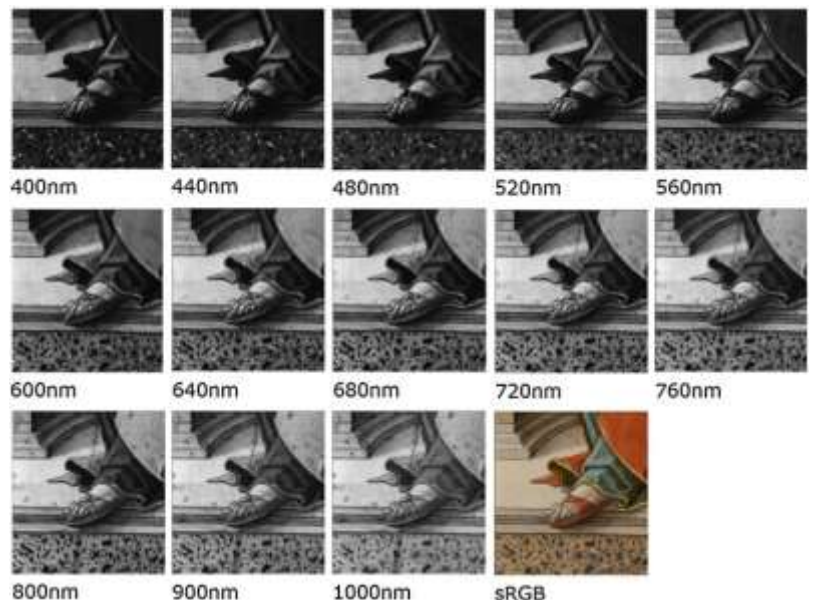


Figure 9: Detail of the painting on the left, acquired in different spectral bands.

#### 1.3.4. X-Ray Fluorescence

In X-Ray Fluorescence (XRF) the sample is irradiated by an intense and focused X-Ray beam. The energy of the X-Rays is sufficient to expel electrons from the inner shells (close to the atomic nucleus) in an atom. Electrons from outer shells fall subsequently into the holes left by the expelled electrons and emit X-Rays in the process. As every atom has its own particular structure of its electron shells, the energy of the emitted X-Rays is characteristic for each element and can be used for its identification.



Figure 10: "Patch of Grass".

A characteristic example of the application of XRF is a painting drawn by Vincent Van Gogh in 1887, named "Patch of grass" (Kröller-Müller Museum, Otterlo, The Netherlands). The red frame in Figure 10 indicates the field of view in Figure 11 (rotated 90° counter-clockwise). The authors of the work report that it is thought that one third of Van Gogh's known paintings seem to hide underneath their paint layers compositions of his early period of creation.

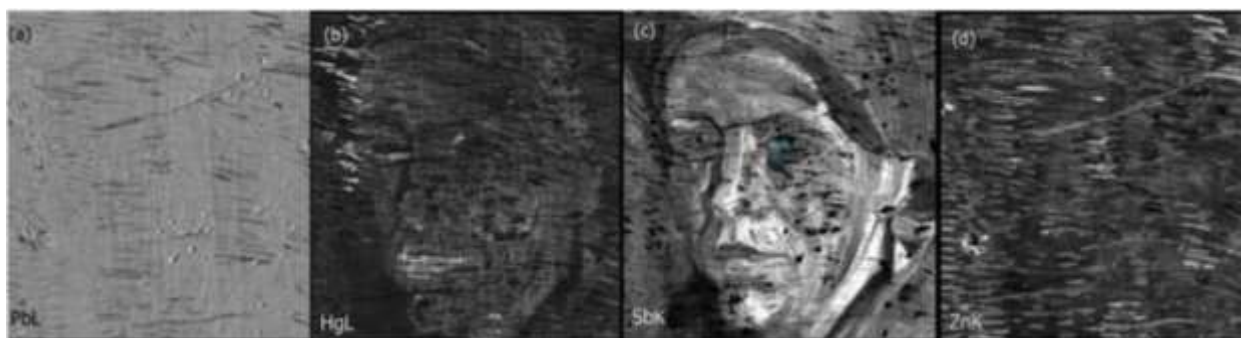


Figure 11: (a) Distribution of Pb L-edge measured with SR-based XRF (black corresponds to low intensity, while white, to high). (b) Hg L-edge indicates the distribution of vermilion. (c) Sb K-edge shows the distribution of Naples yellow, the paint sample location is indicated in the blue frame. (d) Zn K-edge indicates the distribution of zinc white, mostly corresponding with surface painting but some overlap with concentrations of SbK (nose, ear, neck).

### 1.3.5. Optical Coherence Tomography

Optical Coherence Tomography (OCT) is an optical interferometric technique, that is able to provide information about the varnish that exists over the paint layers on an oil painting, as well as about the existence of underdrawings behind the paint layers of a painting, via the creation of a 3-dimensional image of the layers of which the painting is consisted. Specifically, the sample is being irradiated with coherent radiation (usually in the NIR) with high pervasiveness. After, the scattered

radiation from the specimen is detected. OCT has mostly been used in biological applications. Its appearance in cultural heritage took place in the last years and it offers the possibility of a 3-dimensional mapping of the layering of the painting. This way the underdrawing can be distinguished from the paint layers.



Figure 12: "The arrest of Christ".

"The arrest of Christ" is a painting created around 1520 by an anonymous artist. It contains several layers of material, including an underdrawing executed in a dry medium, paint, as well as varnish. Figure 13a shows a single cross-sectional image through the underdrawing feature which lies inside the red square of Figure 12, with three distinct layers visible. From top to bottom, these layers consist of varnish, paint, and underdrawing.

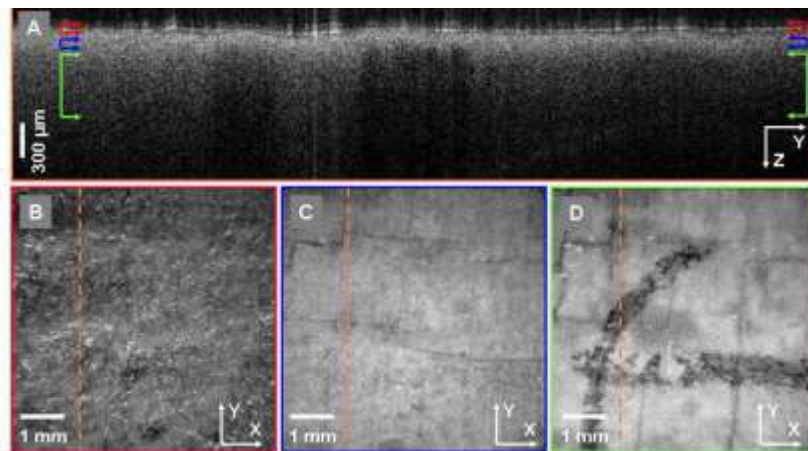
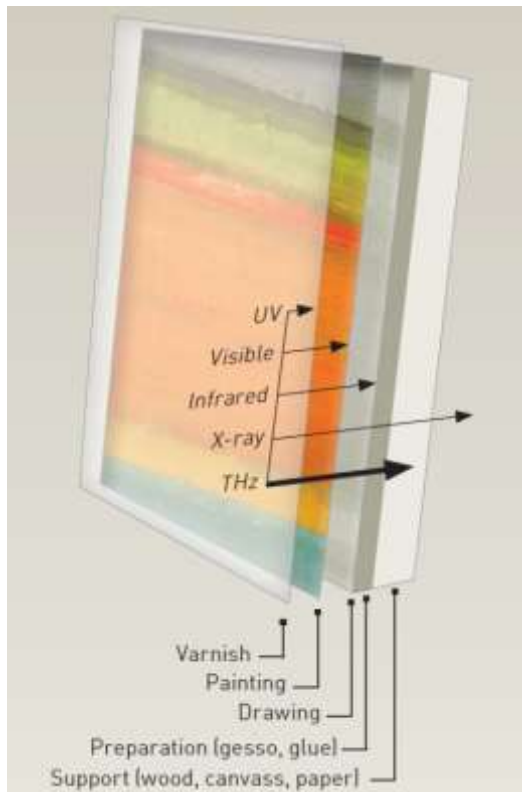


Figure 13: OCT images of the underdrawing feature in "Arrest of Christ." (A) Single cross sectional image taken through the underdrawing. Colored arrows indicate the locations of the varnish (red), paint (blue), and underdrawing (green) layers that were axially summed to form the summed voxel projection en face images in (B)-(D). (B) Summed voxel projection en face image of the varnish layer. (C) Summed voxel projection en face image of the paint layer. (D) Summed voxel projection en face image of the underdrawing layer. Orange dashed line indicates the location of the cross-sectional image in (A).

### 1.3.6. Terahertz Radiation

During the last decades, many research groups have been interested in studying samples in the domain of Terahertz Radiation. It is a nonlinear imaging technique, with wavelengths that lie at the far end of the infrared band, just before the start of the microwave band. The use of this kind of

radiation provides greater penetration in comparison to the IR methods, and due to the fact that the energy of THz photons is lower, and thus more safe, the technique has already been used for many applications. One of the biggest advantages of THz Radiation is that, due to the fact that it consists of



submillimeter waves, it can penetrate through a wide variety of materials such as paper, wood, clothing, plastic and ceramics, which are usually opaque to both visible and infrared radiation. THz Radiation has already been used for the detection of text in papyruses and parchments that had endured severe external damages, for the calculation of the thickness of paint layers in paintings as well as for the detection of cracks on them. In comparison to X-rays and microwaves which can penetrate thick layers and are often used to reveal hidden underdrawings below the painting layers of an artwork, find dislocations, water damages and other defects, THz exhibit better depth and lateral spatial resolution. These transmission properties of the THz radiation in combination with the fact that information can simultaneously be obtained for the internal structure of an artwork, point out the potential of THz waves to become an essential tool for art analysis in the near future.

Figure 14: Cross-section of a typical painting, showing the penetration of different types of electromagnetic radiation. Terahertz rays travel farther into the layers than shorter frequencies of light. Although X-rays penetrate artifacts to greater depths, care must be taken with this ionizing radiation.

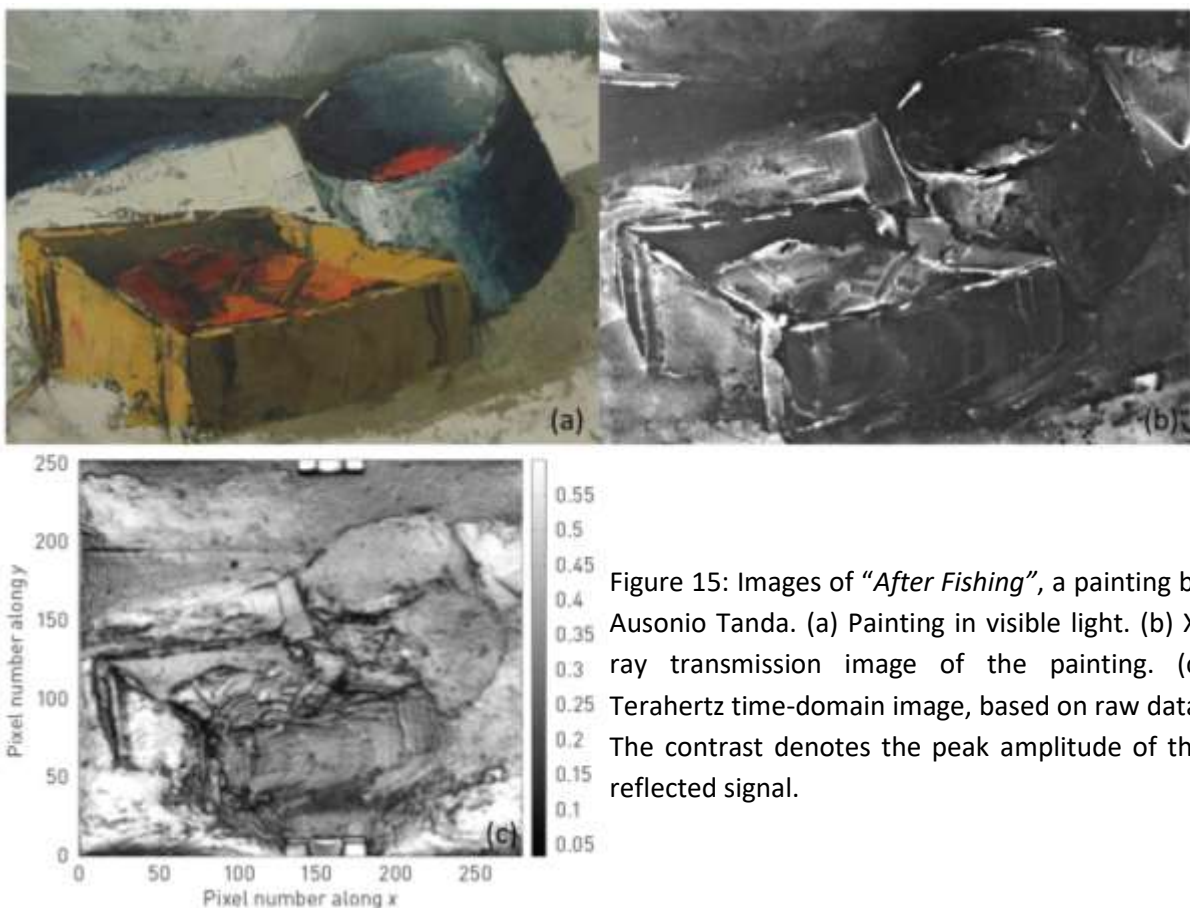


Figure 15: Images of "After Fishing", a painting by Ausonio Tonda. (a) Painting in visible light. (b) X-ray transmission image of the painting. (c) Terahertz time-domain image, based on raw data. The contrast denotes the peak amplitude of the reflected signal.

In Figure 14 is presented an example of the use of the technique on the painting “After Fishing”, made during the 20<sup>th</sup> century by the artist Ausonio Tanda. The artwork consists of thick layers of paint, built up with a palette knife instead of a paintbrush.

### **1.3.7. Limitations of existing techniques**

The aforementioned techniques present certain limitations. The fact that IR Photography, IRR, and MSI are based on the same principles means that these methods face the same constraints. Even though they are widely used for diagnostic purposes on cultural heritage, they are not efficient for a number of applications. To begin with, all these techniques depend on the penetration of IR radiation, which is reduced as the paint layers -and everything else that might exist over the underdrawing, such as binders, varnish etc- increase, due to scattering phenomena. Thus, the absence of underdrawings in a certain area of the imaging with the use of these techniques does not necessarily mean that there is none at the corresponding area of the artwork. This is the main reason why these techniques cannot be used for mural paintings, where the paint layers are, in general, thicker.

The optical limitations due to scattering and reflection of the radiation appear in OCT as well. What is more, OCT can only provide information for the underdrawings after the acquisition of successive measurements and their combination, in order to create the final composition, as each measurement is a perpendicular cross-section (as the one presented in Fig.13A) of the stratigraphy of the artwork. The imaging of underdrawings is thus not the main aim of OCT, as it is a time-consuming and complex process.

THz radiation is a promising technique that has a lot to offer in the field of cultural heritage. A significant challenge of the technique, according to Dr. Jackson, is the fact that there is a relative lack of published standards related to THz spectroscopy. A few THz spectroscopic databases, including one compiled by NICT and other Japanese institutions, exist online, but their entries range in number from a couple dozen to a couple thousand, which means that they are hardly enough to cover all the pigments, binders and residues that an archaeologist or art conservationist might encounter. Establishing standard spectra for materials in any wavelength regime is a challenge full of multi-instrument error analysis and grunt work.

## **2. Theoretical background – tools**

### **2.1. General information**

The PA effect is a phenomenon discovered accidentally in 1880 by A. G. Bell, while he was working on the development of the photophone, a device that allows transmission of speech on a beam of light. Initially the name of the phenomenon was “optoacoustic effect” it was changed though, in order not to be confused with the “acousto-optic effect”, which refers to interactions of light with disturbances that are induced to an acousto-optic crystal because of sound waves. Bell and his partner, S. Tainter, observed that the PA effect is greatly dependent on the absorption of the radiation. What is more, they noticed that the power of the acoustic signal depends on the percentage of light that is being absorbed. Thus, they concluded that the source of the radiation determines the type of sound that is being produced. The PA effect was forgotten though, and it wasn't until after the emergence of lasers, approximately in 1960, when the phenomenon began to be broadly used in different fields.

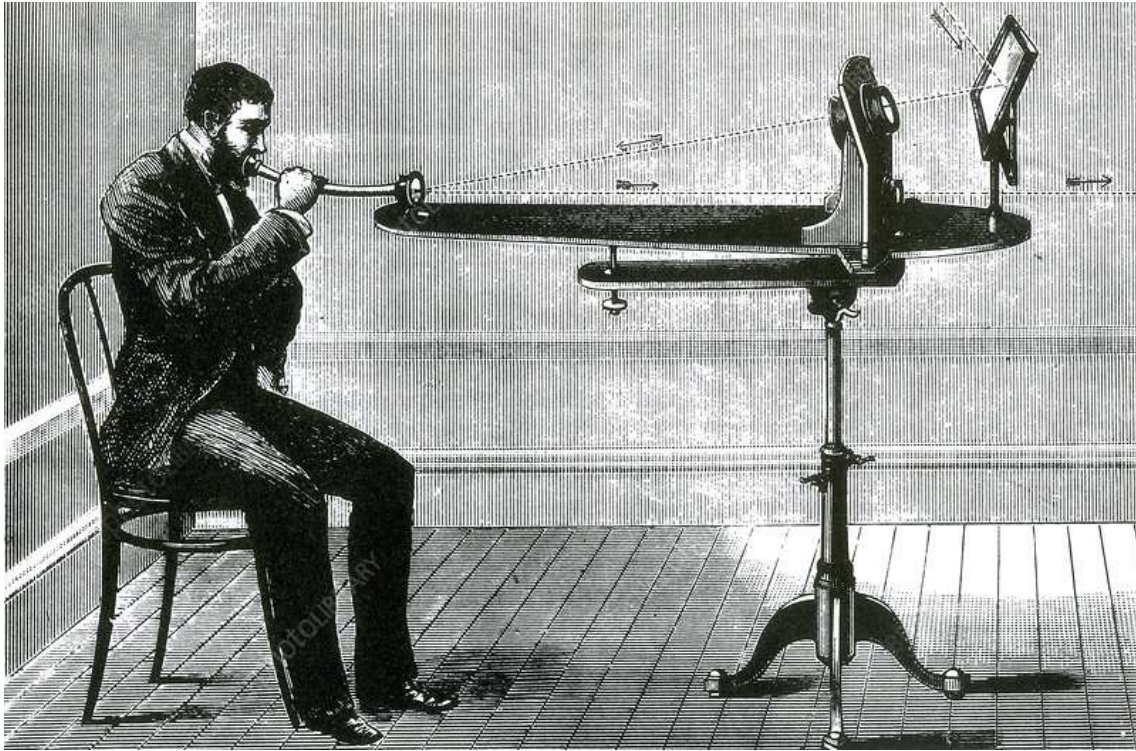


Figure 16: A.G. Bell conducting experiments with the photophone.

Specifically, in 1963 R. M. White discussed about the production of high frequency sound waves in a solid medium as a result of the absorption of electromagnetic radiation. After that, it appeared again in 1967 from M. J. Brienza and A. J. DeMaria, who proved that pulsed Q-switched lasers can be used for the production of intense ultrasound waves during the heating of metal films that were placed on the surface of piezoelectric crystals. Through the irradiation with repetitive ns pulses they managed to produce sound from solids at frequencies higher than 2 GHz. In 1977, R. J. Von Gutfeld and R. L. Melcher proposed for the first time the use of the PA effect as an imaging method, based on White's results. They found that the strength of the acoustic signal could be increased by a large factor if the impedance of the material on either side of the absorbing layer was carefully controlled. They suggested that photoacoustic signals generated in this manner could be used in a system for imaging material defects. Wickramasinghe et al. converted a conventional acoustic microscope into a novel, photoacoustic one, used in transmission mode. The process they followed involved the subtraction of the input acoustic and its replacement by an optical objective lens. In this way, an optical input beam of a mode-locked Q-switched Nd:YAG laser was focused in a circle with a diameter of 2  $\mu\text{m}$ . During the experiments, the sample was being scanned mechanically while the detection of the produced acoustic waves was done with a transducer from the initial microscope. During the time that these experiments took place, the photoacoustic microscopes were being used to detect either the acoustic or the optical image, and not a combination of both. With the use of a photoacoustic microscope adjusted at 50 kHz – 10 MHz, it was possible to produce images through the recording of the thermal waves which were created during the illumination of the sample at areas with different absorbing properties, due to the PA effect. Thus, in 1979 Rosencwaig proposed the idea of a microscope with a system of piezoelectric detection that could provide information about both the surface and the internal structure of the sample.

The PA effect is the production of acoustic waves after the absorption of light with time-variant intensity, in a transmission medium. The amplitude of the produced PA wave is proportional to the fluence of the laser ( $F$ ) and the absorbance coefficient ( $\mu$ ). The amplitude is also determined by the isothermal compressibility ( $\kappa$ ) and the thermal coefficient of volume expansion ( $\beta$ ), which are

thermodynamic constants. The produced waveform depends on the spatiotemporal characteristics as well as on the geometry (e.g. size, shape) of the absorber. The size of the absorber is inversely proportional to the frequency of the PA wave.

## 2.2. Ultrasound propagation

### 2.2.1. Acoustic waves

An acoustic wave is a type of pressure propagation by means of adiabatic compression and decompression. An acoustic wave travels with an acoustic velocity, characteristic of the medium. Acoustic waves are longitudinal and can be described using the following generic properties:

- amplitude ( $s_0$ ): the maximum displacement from the equilibrium
- amplitude of pressure wave ( $p_0$ ): the maximum pressure in comparison to the value at the equilibrium
- speed of sound ( $c$ ): the propagation rate of energy in the transmission medium
- frequency ( $f$ ): the number of cycles completed per second
- intensity ( $I$ ): the emission or absorption rate of acoustic energy per second

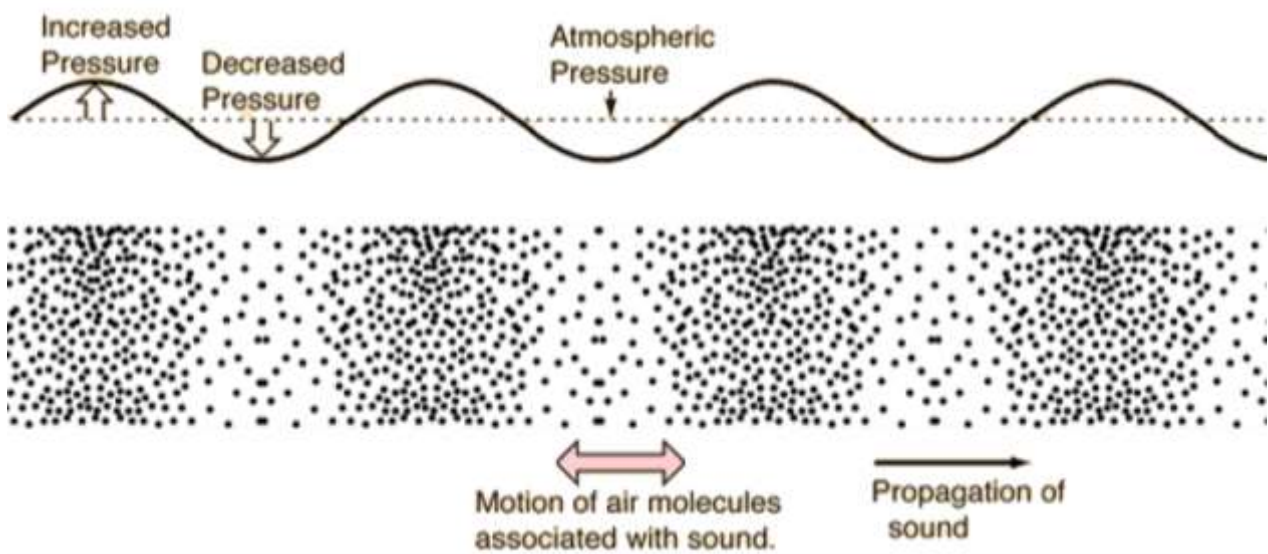


Figure 17: Propagating acoustic wave. In the areas where the density of molecules is high, the pressure is increased, whereas in the areas where the density of molecules is low, the pressure decreases.

Each medium is characterized by its specific acoustic impedance ( $Z$ ), given by equation  $Z = \rho c$  (1), where  $\rho$ : the density of the medium and  $c$ : the speed of sound in it.

Ultrasounds are acoustic waves with frequencies higher than the upper audible limit of human hearing. The frequencies vary from 20 kHz up to several GHz.

### 2.2.2. Reflection and transmission of acoustic waves

When an incident acoustic wave that travels in a medium with specific acoustic impedance  $Z_1$  meets a second medium, with specific acoustic impedance  $Z_2$ , part of the wave is reflected back to the first

medium and the rest refracted into the second medium. Snell's law, which is known for electromagnetic wave propagation, applies in acoustics as well:  $\frac{\sin \theta_i}{\sin \theta_r} = \frac{c_1}{c_2}$  (2).

If  $\theta_i = 90^\circ$  then  $\theta_i = \theta_c$  (critical angle) and  $\sin \theta_c = \frac{c_1}{c_2}$ . What is more, for  $\theta_i > \theta_c$  and  $c_2 > c_1$  the wave is not transmitted into the second medium. The percentage of the  $s_0$  that is being reflected or transmitted is given by the following equations:

$$\text{Transmittance coefficient: } T = \frac{p_t}{p_i} = \frac{2Z_2 \cos \theta_i}{2Z_2 \cos \theta_i + Z_1 \cos \theta_t} \quad (3)$$

$$\text{Reflectance coefficient: } R = \frac{p_r}{p_i} = \frac{Z_2 \cos \theta_i - Z_1 \cos \theta_t}{2Z_2 \cos \theta_i + Z_1 \cos \theta_t} \quad (4).$$

For vertical incidence,  $\theta_i = \theta_t = 0^\circ$  and the above equations can be simplified to:  $T = \frac{2Z_2}{Z_2 + Z_1}$  (5)

and  $R = \frac{Z_2 - Z_1}{Z_2 + Z_1}$  (6). What is more, for every possible pair of angles  $\theta_i$  and  $\theta_t$   $T = 1 + R$  (7).

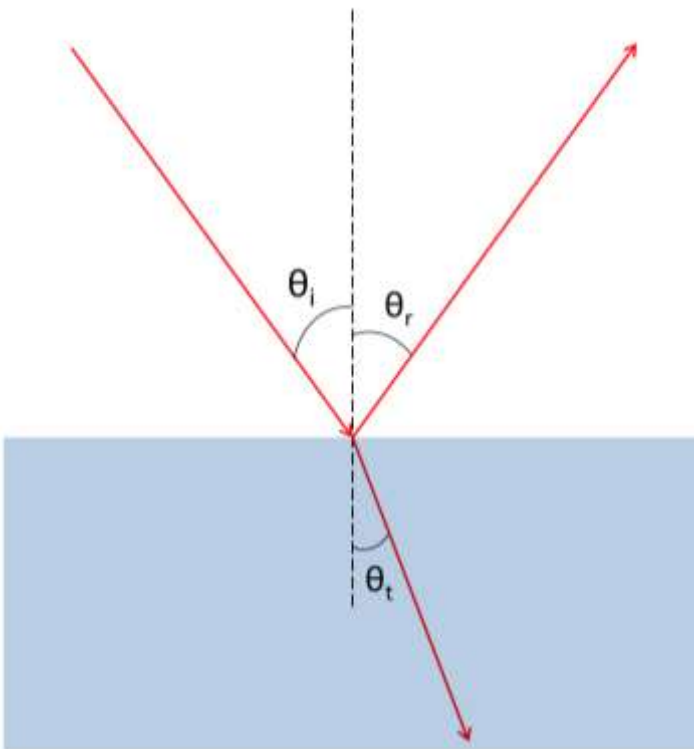


Figure 18: Reflection and refraction of an acoustic wave.  $\theta_i$ : angle of incident acoustic wave,  $\theta_r$ : angle of reflected acoustic wave,  $\theta_t$ : angle of refracted acoustic wave (t stands for transmission, as this part of the wave manages to pass from the first medium to the second).

The percentage of the reflected or transmitted energy is given by equations (8) and (9).

$$R.E. = R^2 = \left( \frac{Z_2 - Z_1}{Z_2 + Z_1} \right)^2 \quad (8)$$

$$T.E. = 1 - R^2 = 1 - \left( \frac{Z_2 - Z_1}{Z_2 + Z_1} \right)^2 \quad (9).$$

When  $Z_2 - Z_1 \approx 1$  (i.e.  $Z_1 \rightarrow 0$ ), it is obvious from equations (8) and (9) that only an insignificant amount of energy manages to pass through the interface.

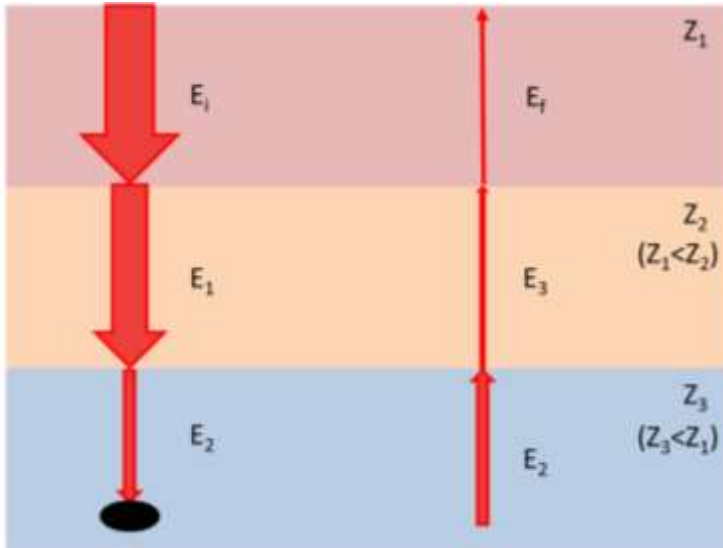


Figure 19: Energy loss in a case where an acoustic wave passes from medium 1, to mediums 2 and 3, is absorbed and reflected and then follows the opposite path, from medium 3 to mediums 2 and 1. In this example it is assumed that there is no energy loss due to absorbance into any medium, and that the absorber reflects 100% of the absorbed energy.

### 2.3. Derivation of the general photoacoustic equation

The PA effect is described by a partial differential equation known as “general photoacoustic equation”, and is derived from two equations.

The first one is the thermal expansion equation:

$\nabla \cdot \vec{\xi}(\vec{r}, t) = -\kappa \cdot p(\vec{r}, t) - \beta \cdot T(\vec{r}, t)$  (10), where  $\vec{\xi}$  represents the medium displacement from the equilibrium state,  $\kappa$  is the isothermal compressibility,  $\beta$  is the thermal coefficient of volume expansion,  $p$  is the pressure and  $T$ , the temperature. Isothermal compressibility is defined as:

$\kappa = -\frac{1}{V} \left( \frac{\partial V}{\partial P} \right)_T$  (11) and expresses the fractional change of volume while changing the pressure at a

constant temperature. Thermal coefficient of volume expansion is defined as:

$\beta = \frac{1}{V} \left( \frac{\partial V}{\partial T} \right)_p$  (12) and it defines how a fraction of volume changes while temperature alters, at a

constant pressure.

In order to extract the second equation we consider a cubic parcel of a medium, with mass  $m$ , equal to  $m = \rho \cdot dA \cdot dz$  (13), where  $dA$  is the infinitesimal surface area,  $dz$  the height and  $\rho$  its density. By replacing (1.4) to Newton’s 2<sup>nd</sup> law we get:

$$F = \rho \cdot dA \cdot dz \cdot a \quad (14).$$

It is also known that  $F = p \cdot A$  (15). Thus, by combining the two equations we get:

$$-dp \cdot dA = \rho \cdot dA \cdot dz \cdot a \Rightarrow -dp = \rho \cdot dz \cdot a \Rightarrow \rho \cdot a = -\frac{dp}{dz} \quad (16).$$

In a more general form, (16) can be written as:

$$\rho \cdot \vec{a} = -\nabla p(\vec{r}, t) \Rightarrow \rho \frac{\partial^2}{\partial t^2} \vec{\xi}(\vec{r}, t) = -\nabla p(\vec{r}, t) \quad (17).$$

Taking the divergence of (17):

$$\rho \frac{\partial^2}{\partial t^2} [\nabla \cdot \vec{\xi}(\vec{r}, t)] = -\nabla^2 p(\vec{r}, t) \quad (18).$$

Eq. (18) is called inviscid force equation.

$$(10), (18) \Rightarrow \rho \frac{\partial^2}{\partial t^2} [-\kappa p(\vec{r}, t) + \beta T(\vec{r}, t)] = -\nabla^2 p(\vec{r}, t) \quad (19).$$

If we arrange the terms more conveniently, we obtain:

$$\left( \nabla^2 - \rho \kappa \frac{\partial^2}{\partial t^2} \right) p(\vec{r}, t) = -\beta \rho \frac{\partial^2 T(\vec{r}, t)}{\partial t^2} \quad (20).$$

From the Newton-Laplace equation we can derive the speed of sound:

$$u_s = \sqrt{\frac{K}{\rho}} \quad (21),$$

where K is the bulk modulus measuring the resistance of the medium to uniform compression. K is equal to the inverse compressibility  $\kappa$ . Thus, the speed of sound can be expressed

$$\text{as } u_s = \sqrt{\frac{1}{\rho \kappa}} \quad (22).$$

The final form of the photoacoustic equation is a result of the combination of (20) and (22) and is shown below:

$$\left( \nabla^2 - \frac{1}{u_s^2} \frac{\partial^2}{\partial t^2} \right) p(\vec{r}, t) = -\frac{\beta}{\kappa u_s^2} \frac{\partial^2 T(\vec{r}, t)}{\partial t^2} \quad (23).$$

The left side of the equation describes the pressure wave propagation. The right side is the source term. We can easily conclude from the equation that time-invariant heating does not produce a pressure wave, only time-variant heating does.

## 2.4. Photoacoustic equation under thermal confinement

Under thermal confinement conditions, at which heat conduction is negligible during the laser pulse, we can derive from the fundamental equation  $Q = mC_v T$  (24) (where Q: thermal energy, m: mass,  $C_v$ : specific heat capacity under constant volume and T: absolute temperature) that:

$$\frac{dQ}{dt} = mC_v \frac{dT}{dt} = \rho V C_v \frac{dT}{dt} \quad (25).$$

We define the heating function  $H$  (Enthalpy) as the thermal energy converted per unit volume per unit time (S.I. units:  $\frac{J}{m^3 s}$ ). From (25):

$$H = \rho C_V \frac{dT}{dt} \quad (26).$$

It is also known from thermodynamics that:

$\frac{C_P}{C_V} = \frac{\kappa}{\beta_s}$  (27), where  $C_P$  and  $C_V$  are the specific heat capacities under constant pressure and volume, while  $\beta_s$  stands for the isentropic compressibility, which is defined as

$$\beta_s = -\frac{1}{V} \left( \frac{\partial V}{\partial P} \right)_s \quad (28).$$

On the other hand, the equation of state (which gives us information about the relation of the thermodynamic variables) denotes that:

$$u_s^2 = \left( \frac{\partial P}{\partial \rho} \right)_s \quad (29).$$

By combining (28) and (29) we get:

$$\beta_s = -\frac{1}{V} \left( \frac{\partial V}{\partial P} \right)_s \frac{\partial \rho}{\partial \rho} = -\frac{1}{V} \left( \frac{\partial \rho}{\partial P} \right)_s \frac{\partial V}{\partial \rho} = -\frac{1}{Vu_s^2} \frac{\partial V}{\partial \rho} = -\frac{1}{Vu_s^2} \frac{\partial(m/\rho)}{\partial \rho} = \frac{1}{\rho u_s^2} \quad (30).$$

(27) and (30) will finally result in:

$$\kappa = \frac{C_P}{\rho u_s^2 C_V} \quad (31).$$

By substituting (24) and (31) to (23), the source term (right part) becomes:

$$-\frac{\beta}{\kappa u_s^2} \frac{\partial^2 T(\vec{r}, t)}{\partial t^2} = -\frac{\beta}{C_P} \frac{\partial H(\vec{r}, t)}{\partial t} \quad (32).$$

Thus, we conclude: 
$$\left( \nabla^2 - \frac{1}{u_s^2} \frac{\partial^2}{\partial t^2} \right) p(\vec{r}, t) = -\frac{\beta}{C_P} \frac{\partial H(\vec{r}, t)}{\partial t} \quad (33).$$

From the form of the equation we can derive a result of significant importance; it is obvious that for the production of a propagating pressure wave, a time-varying source of irradiation is needed. Otherwise, the right hand side of the equation (33) would be equal to zero, and thus, the photoacoustic effect wouldn't take place.

The quantity  $H(\vec{r}, t)$  can be further decomposed as the product of the respective spatial and temporal parts (separation of variables) in the following form:

$H(\vec{r}, t) = H_s(\vec{r})H_T(t)$  (34), where  $H_s(\vec{r})$  represents the local deposited energy density in  $\text{J/m}^3$  and  $H_T(t)$  is the temporal excitation profile.

Using eq. (34), (33) can be written as:

$$\left( \nabla^2 - \frac{1}{u_s^2} \frac{\partial^2}{\partial t^2} \right) p(\vec{r}, t) = - \frac{\beta H_s(\vec{r})}{C_p} \frac{\partial H_T(t)}{\partial t} \quad (35)$$

Equation (35) compromises the photoacoustic equation under thermal confinement conditions.

Each laser pulse can be ideally considered as a delta function. In this case (35) is written as:

$$\left( \nabla^2 - \frac{1}{u_s^2} \frac{\partial^2}{\partial t^2} \right) p(\vec{r}, t) = - \frac{\beta H_s(\vec{r})}{C_p} \frac{\partial \delta(t)}{\partial t} \quad (36).$$

This is the final form of the photoacoustic equation.

## 2.5. Requirements of effective heat production

From equation (10) we can conclude that if the laser pulse width is much shorter than both the thermal and stress relaxation time (no heat or stress escapes), the fractional volume expansion will be negligible; therefore the left part of (10) can be set equal to zero. Immediately after the laser pulse, assuming homogeneous illumination, the local pressure rise ( $p_0$ ) can be derived as:

$$p_0 = \frac{\beta T}{\kappa} \quad (37).$$

Using (24), equation (37) can be further re-written in a temperature-independent form:

$$\Delta Q = mC_v \Delta T \Rightarrow \frac{\Delta Q}{V} = \rho C_v \Delta T \Rightarrow \Delta T = \frac{\Delta Q}{\rho C_v V} \quad (38)$$

The ratio  $Q/V$  reflects the thermal energy converted per unit volume and can be expressed as a function of the specific optical absorption  $A$ , which determines the amount of absorbed laser light per volume unit (S.I. units:  $\text{J/m}^3$ ). Thus,

$$\frac{\Delta Q}{V} = \eta_{th} A \quad (39). \quad \eta_{th} \text{ corresponds to the percentage of the absorbed optical energy that is converted}$$

into heat. Thus, we extract from (38) that:

$$\Delta T = \frac{\eta_{th} A}{\rho C_v} \quad (40).$$

By combining equations (37) and (40):

$$p_0 = \frac{\beta}{\kappa \rho C_v} \eta_{th} A \quad (41).$$

Using (31) and (41), the initial photoacoustic pressure is expressed as

$$p_0 = \frac{\beta u_s^2}{C_p} \eta_{th} A \quad (42).$$

In order to simplify the calculations, we define  $\Gamma \equiv \frac{\beta u_s^2}{C_p}$  (43) as the dimensionless Grueneisen parameter  $\Gamma$  and thus, (42) becomes  $p_0 = \Gamma \eta_{th} A$  (44).

If we consider stress confinement, the initially generated photoacoustic pressure will be proportional to  $H_S(\vec{r})$  function, with proportionality constant the Grueneisen parameter  $\Gamma$ , which we previously defined. Thus, it is obvious from (42) and (43) that:

$$H_S(\vec{r}) = \eta_{th} A \quad (45).$$

By substituting the specific optical absorption  $A$  for the product  $F\mu_a$ , where  $F$  is the optical fluence ( $\text{J}/\text{cm}^2$ ) and  $\mu_a$  corresponds to the optical absorption coefficient ( $\text{cm}^{-1}$ ) for the employed wavelength, (44) can be re-written as:

$$p_0 = \Gamma \eta_{th} \mu_a F \quad (46).$$

By assuming uniform absorption properties of the object,  $H_S(\vec{r})$  can be finally written as:

$$H_S(\vec{r}) = \eta_{th} \mu_a F(\vec{r}) \quad (47).$$

## 2.6. Spotsize and fluence calculation

The energy of the beam was measured using a joulemeter. For the measurement, a diverging lens and the measuring instrument were placed right after the converging lens of the apparatus. The energy was found equal to  $E = 1.73 \text{ mJ} \pm 19.9 \text{ } \mu\text{J}$ . The spot of the laser beam is elliptical, with axes  $a = 1.2 \text{ mm}$  and  $b = 0.6 \text{ mm}$ . Using equation  $s = \pi ab$  (48), where  $s$ : the area of the ellipse, the spotsize of the laser beam equals to  $2.3 \text{ mm}^2$ . Thus, the fluence can be calculated using equation

$$F = \frac{E}{s} \quad (49) \text{ and is found equal to } 75.22 \text{ mJ}/\text{cm}^2 \pm 0.01 \text{ mJ}/\text{cm}^2.$$

## 2.7. Spatial resolution

The property that sets the spatial resolution is the impulse response of the imaging system or, more accurately, the characteristics of the image obtained when scanning an isolated point target. The obtained image in this case depicts a map of the combined effect of the physical processes involved and the reconstruction procedure. This map is known as the point spread function (PSF).

The profile of the PSF along any direction depicts the “smearing” of the information along that direction due to the overall reconstruction process. In the context of PAI, it is important to characterize the resolution along the beam direction, defined herein as the “axial resolution” and the resolution perpendicular to the beam, defined as the “lateral resolution”.

Since the optical beam -even in the absence of scattering- is much wider than the acoustic focus, the lateral resolution of the system is given by  $R_L = 0.71 \frac{\lambda_A}{NA_A} = 0.71 \frac{v_A}{NA_A f_A}$  (50), where  $NA_A$  is the numerical aperture of the ultrasonic transducer,  $v_A$  is the speed of sound in the medium, and  $\lambda_A, f_A$

are the central wavelength and frequency of the PA signal, respectively. The constant 0.71 reflects the full width at half maximum (FWHM) of the acoustic focal spot in acoustic amplitude. In the case our system, the bandwidth of the produced signal is wider than the transducer's. Thus, for the calculation of the lateral resolution is defined by the central frequency of the transducer, which is  $f_c = 73\text{MHz}$ . Its diameter (d) is equal to 4mm and the focal length (f) is 4.53mm. The numerical aperture of the transducer is:  $NA_A = \sin \theta \approx \theta = \frac{d/2}{f} = 0.442$ . What is more, the speed of sound in water (for 25°C) is 1498m/s.

Hence, the diffraction limited value of the lateral resolution of our system is:  $R_L = 33\mu\text{m}$ .

For the computation of the axial resolution we use equation  $R_A = 0.88 \frac{v_A}{\Delta f_A}$  (52), which is based on the assumption that the PA response to a point target follows a Gaussian frequency profile.  $\Delta f_A$  is the PA signal bandwidth, which can be approximated as the detection bandwidth of the ultrasonic transducer and is often proportional to its central frequency  $f_A$ . It is also known that high frequency components of acoustic waves are attenuated faster than low frequency ones, and thus, the PA signal bandwidth decreases with imaging depth, resulting in worse axial resolution at greater depths.

For our transducer  $\Delta f_A \sim 10^8$  Hz, so the axial resolution of the system is:  $R_A = 13.18\mu\text{m}$ .

## 2.8. The Nyquist-Shannon Theorem

One of the most important rules of sampling is called “The Nyquist-Shannon Theorem”. This theorem states that the highest spatial frequency of the specimen which can be represented accurately while preserving spatial resolution in the resulting digital image is one half of the sampling rate. The Nyquist rate specifies the minimum sampling rate that fully describes a given signal; in other words a sampling rate that enables the signal's accurate reconstruction from the samples. In reality, the sampling rate required to reconstruct the original signal must be somewhat higher than the Nyquist rate, because of quantization errors introduced by the sampling process. As a result, if the sampling occurs at an interval beneath the number required by the Nyquist criterion, details with high spatial frequency will not be accurately represented in the final digital image.

## 2.9. Absorbance spectrums

Considering that the transmission (T) for thick layers is zero, as the photons cannot reach the rear side of the sample, we can write that  $R + A = 1$  (53), where R stands for reflectivity and A for absorbance. Thus, if the pigment used in the samples has a low value of reflectivity, it is more probable that a number of photons will achieve to reach the depth of the underdrawing, as they are absorbed not only at the interface of the sample and the environment, but also inside the volume of the pigment. The pigments that were used for the preparation of the samples have a reflectivity between 58% and 93% at 1064nm.

Below are given the graphs [Fig. 19-22] of the reflectance spectrums of the pigments used in the samples.

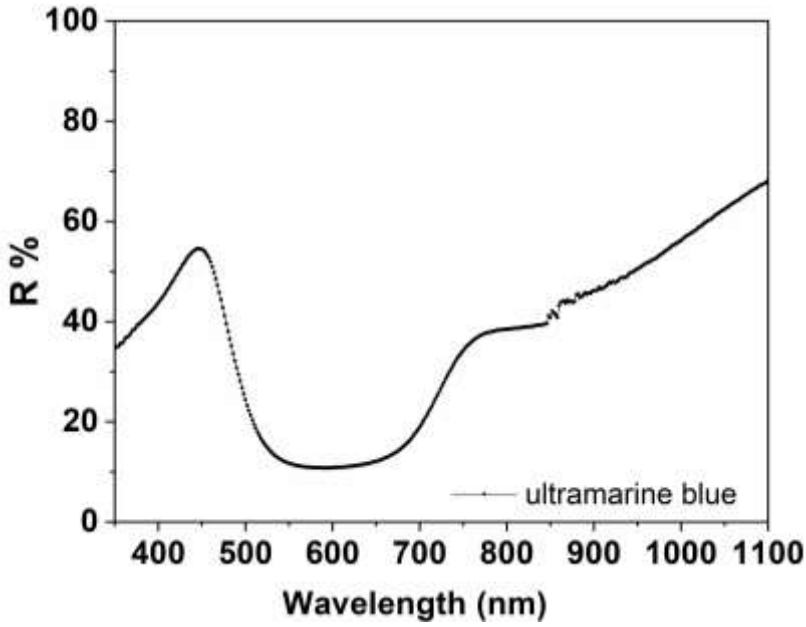


Figure 20: Reflectance spectrum of ultramarine blue.

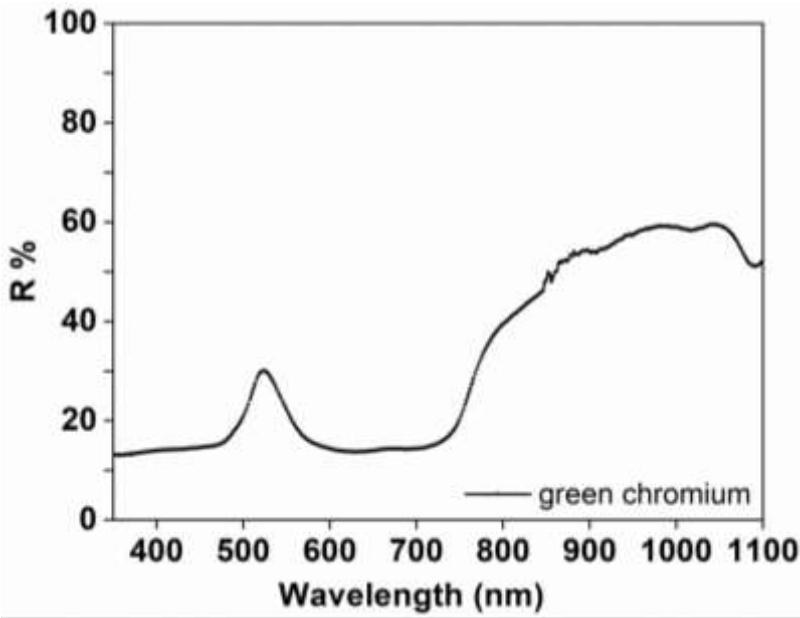


Figure 21: Reflectance spectrum of chromium green.

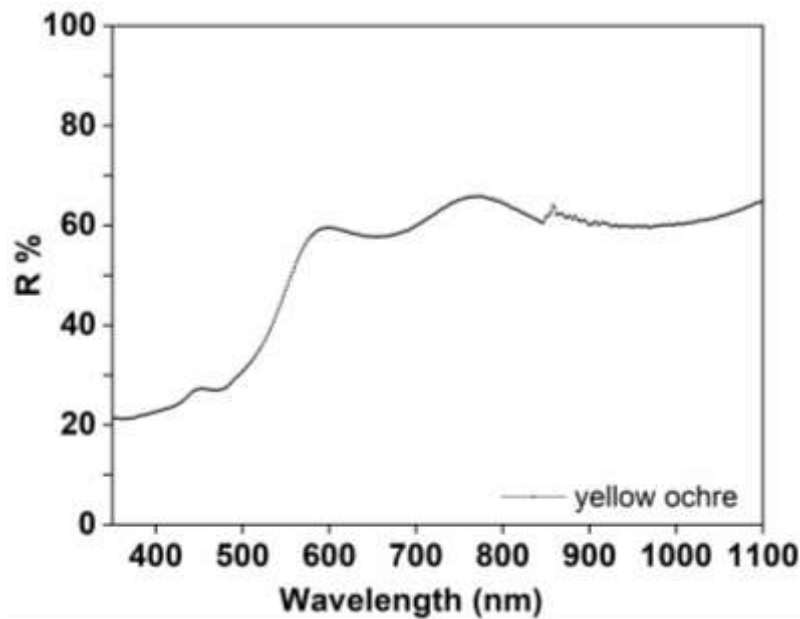


Figure 22: Reflectance spectrum of yellow ochre.

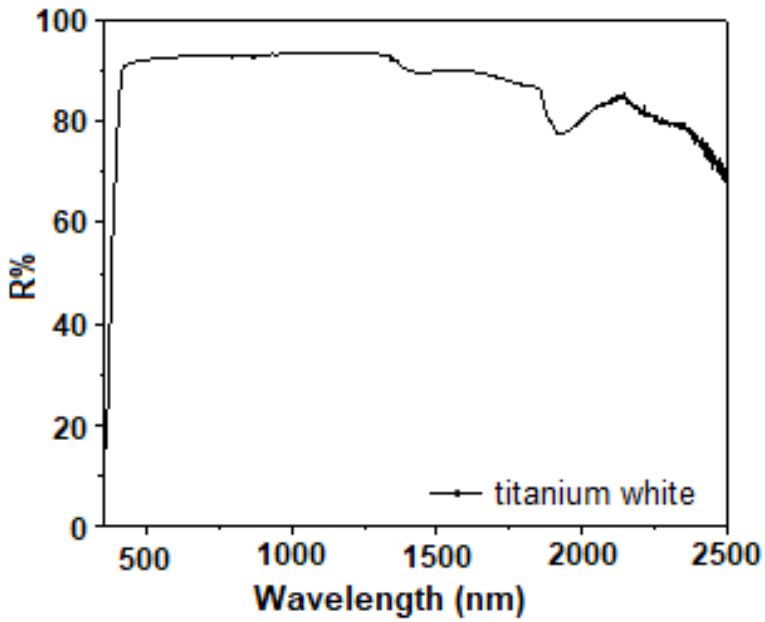


Figure 23: Reflectance spectrum of titanium white.

### 3. Experimental setup

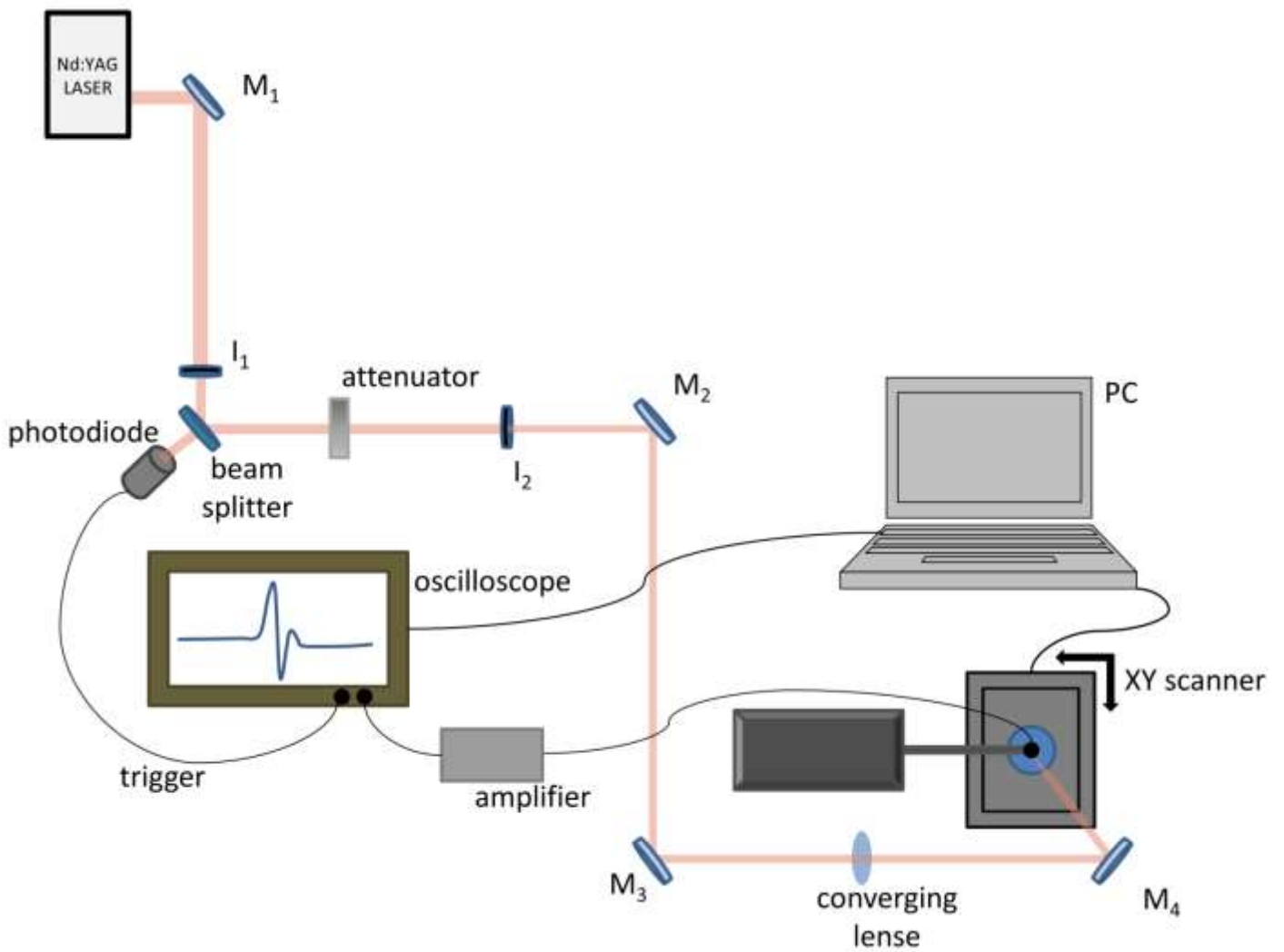


Figure 24: Visual representation of the experimental setup ( $M_i$ : mirrors,  $I_i$ : irises)

The experimental apparatus [Fig.24] employs a Q-switched Nd:YAG laser source emitting infrared radiation at 1064 nm, with pulse duration equal to 10 ns. The selected Repetition Rate [RR] is 10 Hz. Before the irradiation of the sample, the beam is split by a beam-splitter. A percentage is lead to a photodiode in order to acquire trigger and the rest passes through an attenuator. The energy is thus reduced to a level that is not destructive for the pigment of the sample. Before the irradiation, the beam is focused by a converging lens ( $f=50\text{cm}$ ). The sample is placed at the bottom of a Petri dish which is filled with distilled water, which acts as the coupling medium, in order to ensure efficient transmission of the ultrasound signals that are induced by the laser. The Petri dish is attached to a high-precision motorized XY micrometric stage, which can scan a square area up to  $56.25\text{cm}^2$ . The precession of the stage's step is under a  $\mu\text{m}$ . For the detection of the generated photoacoustic waves, a single element spherically focused broadband ultrasonic transducer (HFM28, SONAXIS, Besancon, France; central frequency: 73MHz, focal distance: 4.53 mm) is immersed in the distilled water. The acquired time-domain signal is enhanced using low two noise RF amplifiers, connected series (gain: 64 dB) and is then transmitted to an oscilloscope (Agilent Technologies) and recorded by a computer, using custom-made scripts.

In order to improve the Signal to Noise Ratio (SNR), for each measurement sequential photoacoustic waveforms were averaged over 2 to 8 incident laser pulses, depending on the stability of the acquired signal.

## 4. Methods

### 4.1. Sample preparation

Each sample has a geometric pattern or a plain drawing on the prepared gypsum substrate, coated with a thin layer of paint. The gypsum is combined with a hardener and the mixture is placed in a round vessel (usually not larger than 6cm in diameter) and left to dry for a couple of days. Then, the pattern that represents the hidden underdrawing of the mural is drawn, using a graphite pencil (Faber-Castell (B), Stein, Germany). Subsequently, one or two characteristic types of pigment are mixed with an acrylic binder (Lascaux Acrylic Adhesive 498 HV) and in some cases with gypsum, in order to form thick acrylic paints. Each paint paste was applied with the use of a paintbrush over the sketches, forming paint layers whose thickness was a few hundred  $\mu\text{m}$ .

The pigments that were used for the samples are Ultramarine Blue (Kremer 4503), Chromium Green (Kremer 4432), Titanium white (Kremer 46200), Ochra Yellow (Kremer4800) and Minium (Kremer42500).



Figure 25: Representation of a typical sample.

## 4.2. Acquisition

In order to acquire the PA signal, the water-immersion transducer is submerged into the Petri Dish that contains the sample and is filled with distilled water. Afterwards, the transducer is moved until it is accurately focused. The transducer scans a square area of the sample, whose surface is defined by the user. The measurement begins with the transducer being at the top left corner of the sample, and then, it is raster scanned, with the help of the motorized stages.

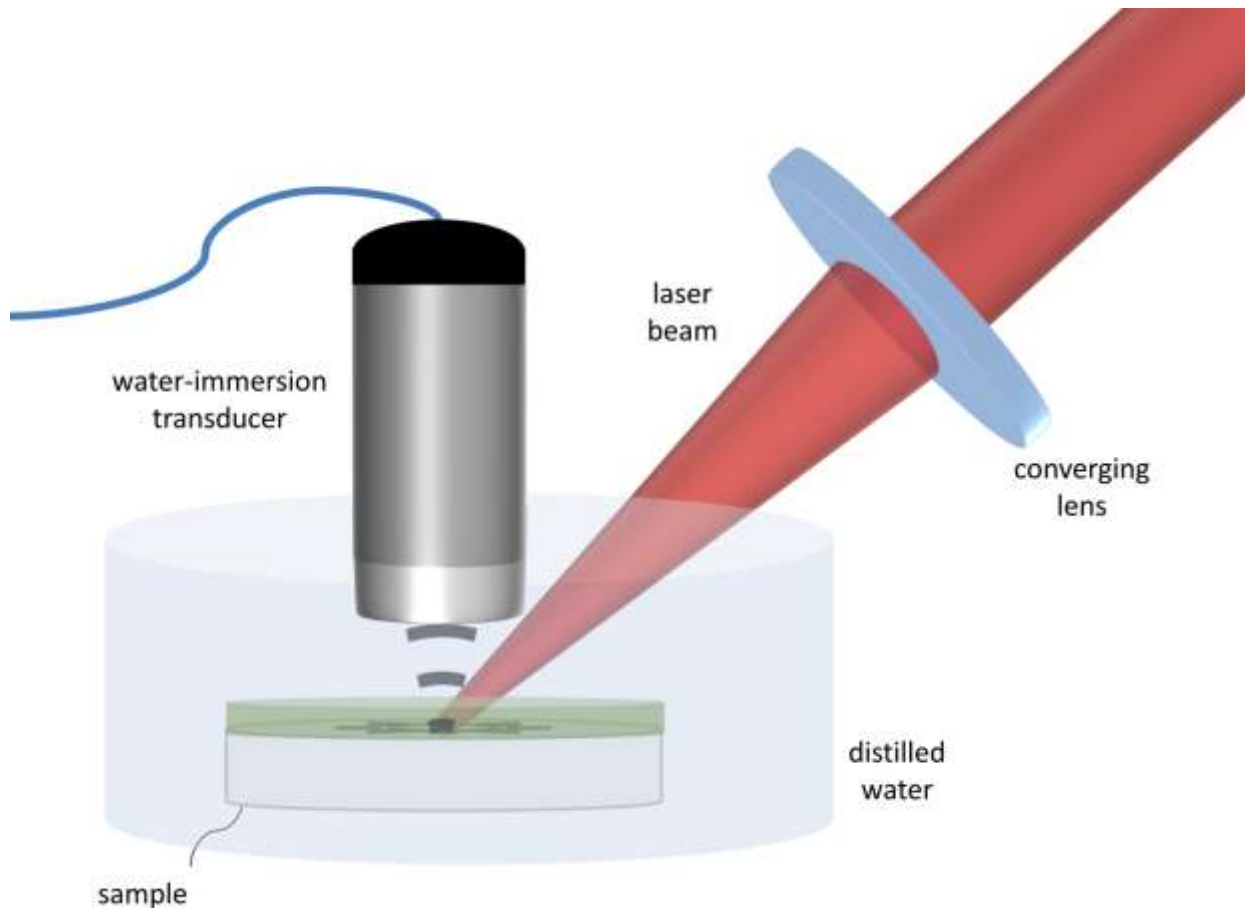


Figure 26: Visual representation of a sample being illuminated by the laser beam and the transducer being submerged into the distilled water, during the measurement.

## 4.3. Data analysis

The recorded waveforms are averaged two times in order to improve the signal to noise ratio (SNR), transferred to a computer and where the signal is filtered, by cutting-off frequencies higher than 30MHz -for high frequency noise elimination- as well as frequencies lower than 100kHz, before the estimation of the peak-to-peak PA amplitude value. The initial unprocessed 8-bit images are created using these peak-to-peak PA amplitude values. Regardless of the scanned area, the pixel size was kept constant to 0.3mm/pixel (e.g. for a 30x30mm<sup>2</sup> area, the obtained image is 100x100 pixels).

For the acquisition of the PA image a MATLAB environment was used. As it is shown at the Figure 26, the user can choose the parameters that best apply to the requirements of each sample.

During the measurements that took place for the needs of this work, the parameters were set as shown on Table 1.

**Table 1: Typical values of the parameters**

time window ( $\mu\text{s}$ )	2.0
temporal delay ( $\mu\text{s}$ )	3.9 – 4.5
number of averages	2
acquired points	1000
trigger level (V)	2.0
length of square side (mm)	25 – 30
number of pixels	84 – 100

Parameter explanation:

The time window represents the time domain from which the amplitude is acquired. The information of one pixel that appears in the final image is the result of the averaging of two signals. The temporal delay expresses the time needed for the ultrasound to travel from the underdrawing to the transducer. The acquired points are the number of points used to recreate the waveform, in the corresponding time window. The recording of the PA signal has to start when the photodiode measures a signal equal or bigger than the value of the trigger level in order to match the PA signals with each pulse.

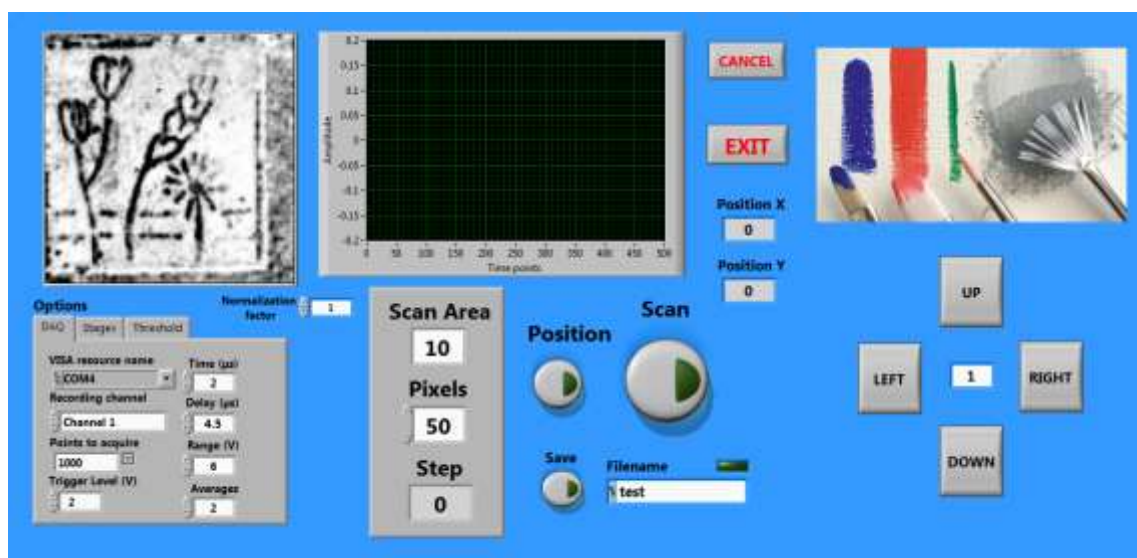


Figure 27: Screenshot of the environment used for the acquisition of the PA images.

## 5. Results

As mentioned in 1.3.2., IR is a technique broadly used in diagnostics of artworks. In order to prove the importance of our work, images of the underdrawings of the samples were obtained with the MSI system of the IESL (IRIS-II) as well, in a spectral range between 1000–1200nm, with a view to comparing the two methods. In most cases, the contrast of the PA was higher than the one obtained by the IR. The samples were divided in two groups.

### 5.1. Chromium Samples

A set of five samples whose paint layers are composed of Chromium Green and Titanium White, but differ in their thickness were measured successively using both PAI and MSI, in order to observe and

quantify the change of the contrast in relation to the different thicknesses, as well as to compare the results of the two imaging methods.

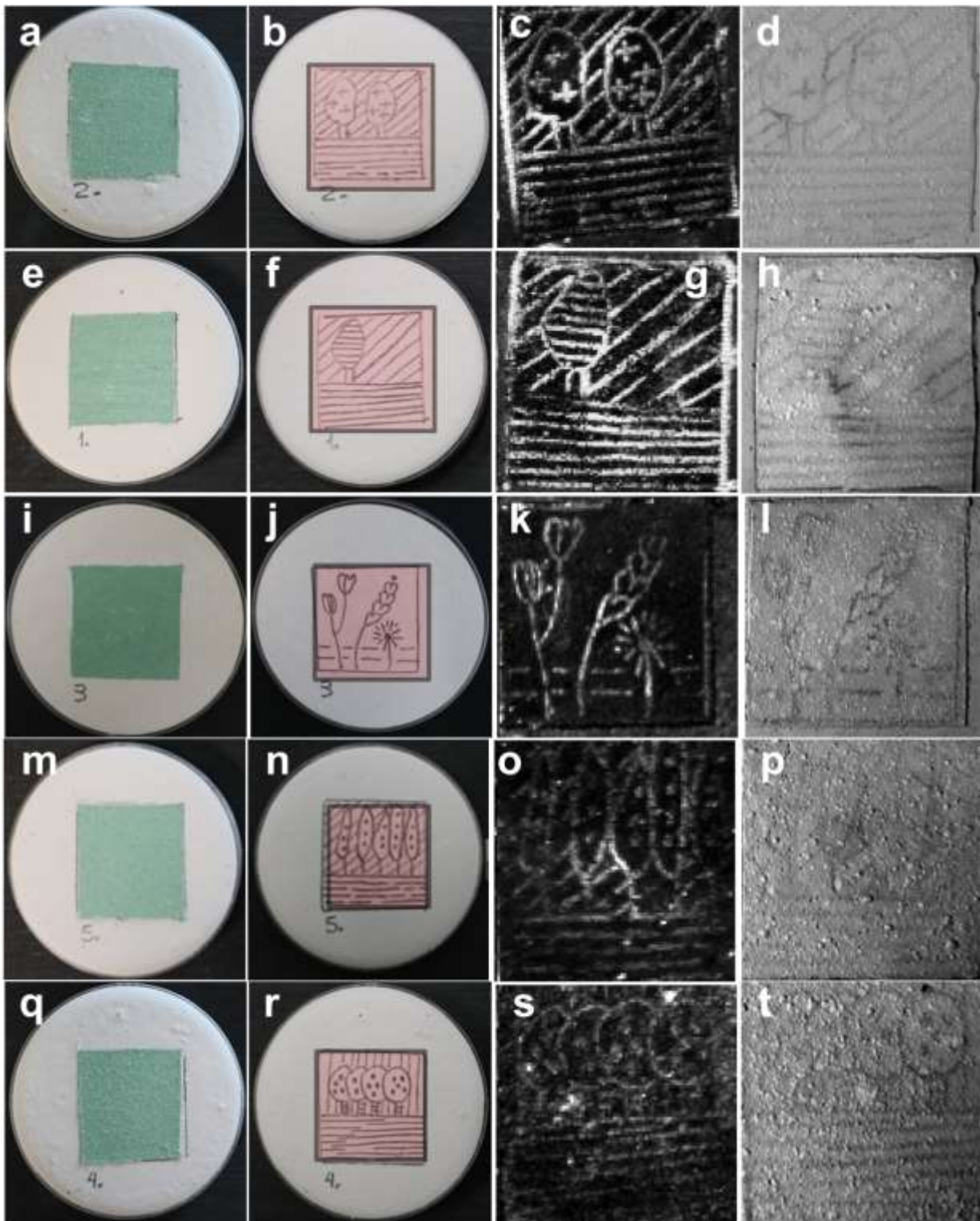


Figure 28: Images a, e, i, m: brightfield views of the samples. Images b, f, j, n, r: brightfield views of the underdrawings of the samples on their left. Images c, g, k, o, s: recovered patterns of the initial underlying sketch through PAI. Images d, h, l, p, t: images acquired through IR, with a filter at 1100nm. In all cases, the processed image is presented. The thickness of the paint layer increases as we move towards the bottom.

It is obvious that the underdrawings are not visible to the naked eye in any of the samples (Figure 28 a, e, l, m, q). Also, it is clear that the PAI is not limited by the artefacts of the surface of the samples, such as the undissolved gypsum that is present into the paint layer, in the same degree with the MSI where each grain creates a dark region around it. In order to compare the results objectively, the contrast (C) of each image was calculated, using the formula:

$$C = \frac{A_{graph} - A_{paint}}{A_{graph} + A_{paint}} \quad (54),$$

where  $A_{graph}$  and  $A_{paint}$  are the peak-to-peak PA amplitudes for graphite and the overlying paint layer, respectively.

Before the calculation, the raw data was processed using ImageJ. Each image had its contrast enhanced by saturating 0.3% of the total pixels.

What is more, the profiles of the samples were acquired with a profilometer and after, with the use of a MATLAB script, the mean thickness of each sample was measured.

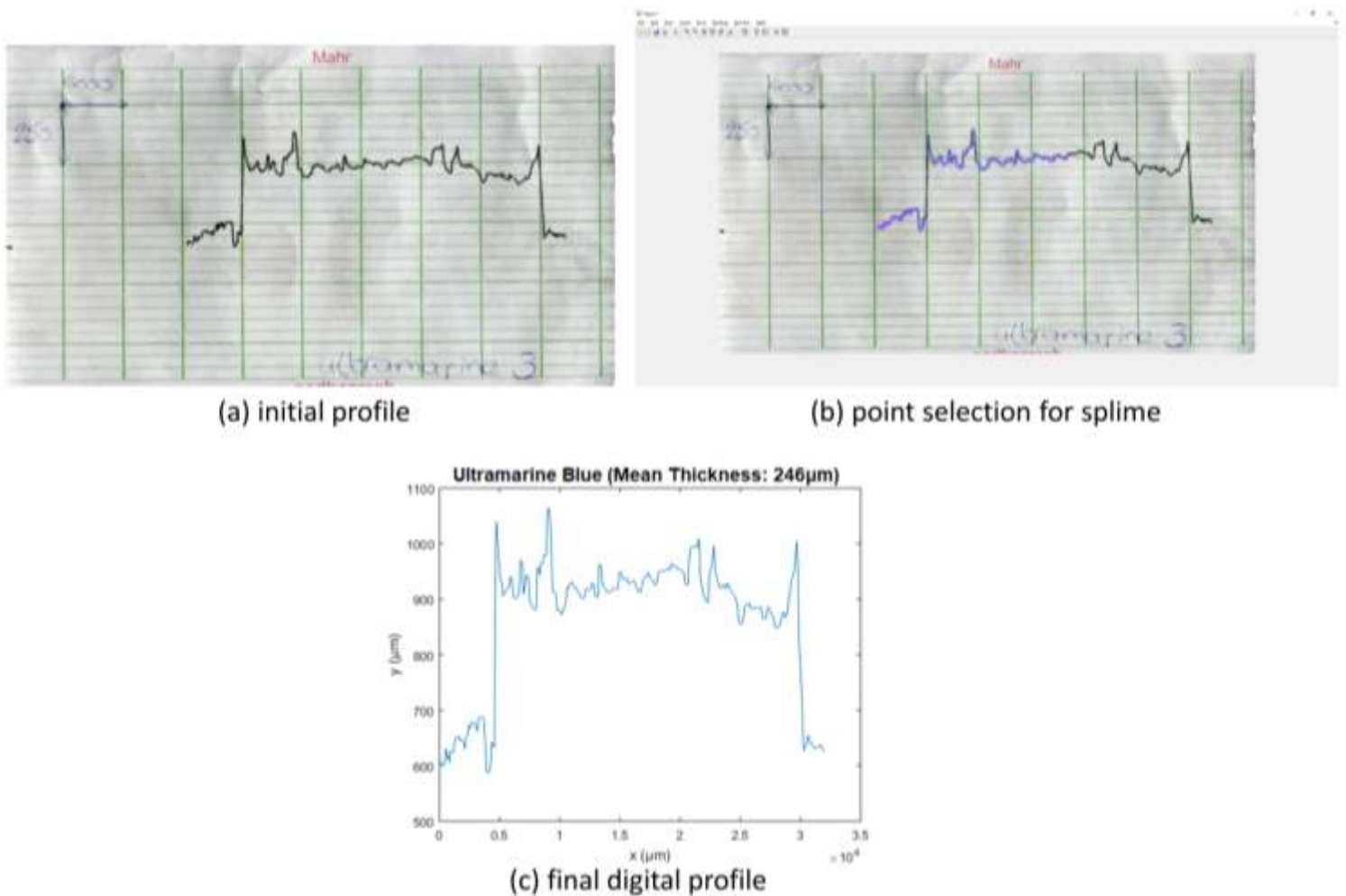


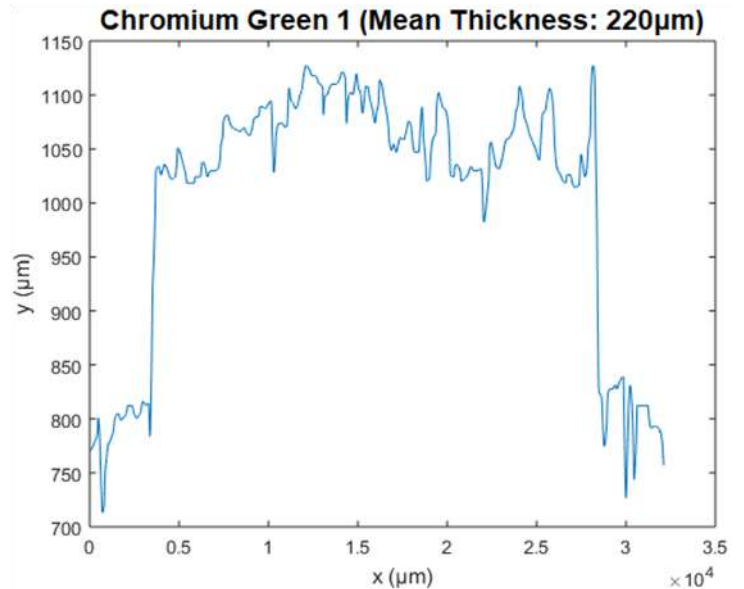
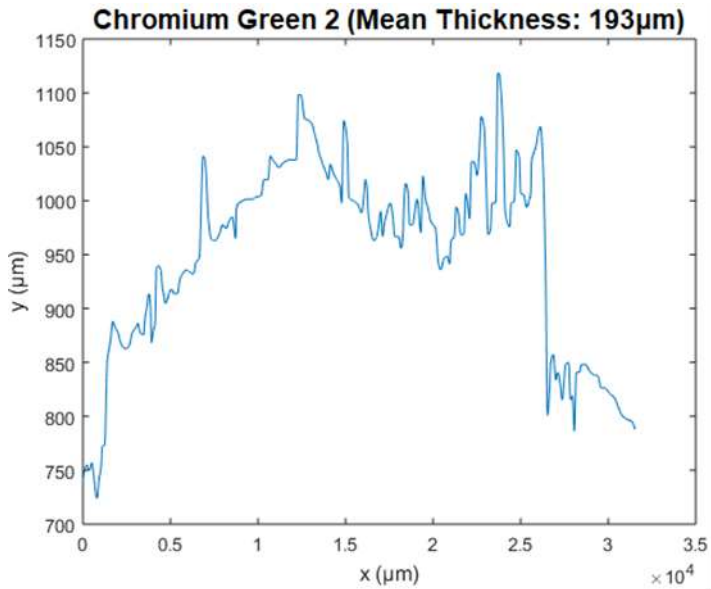
Figure 29: The transition from the initial (a), to the final digital profile (c) with the use of a spline.

The values of the chromium samples range between 193–257  $\mu\text{m}$ . They are listed in Table 2. The profiles of the samples are presented in Figures 30–34.

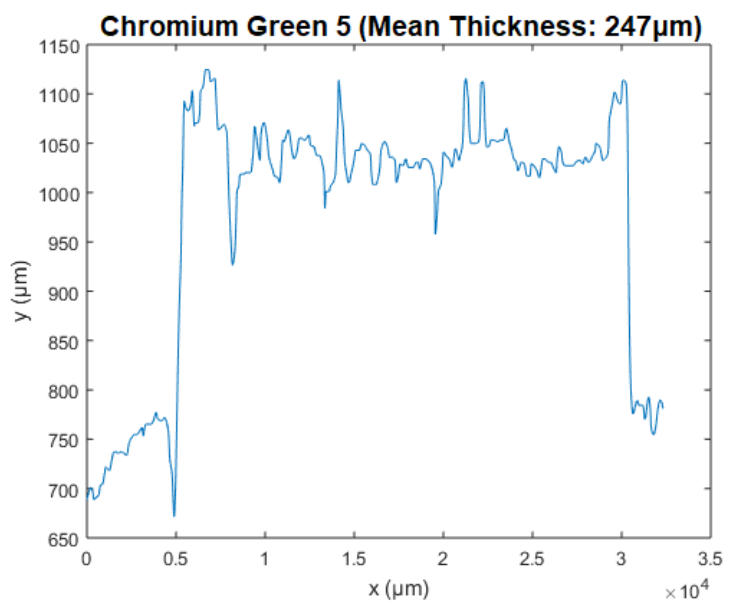
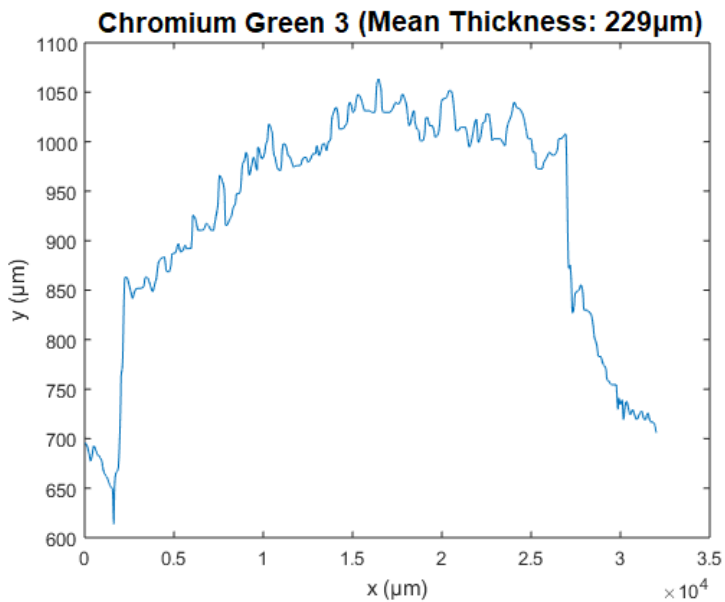
In order to get a more reliable value for the contrast of each sample, the values displayed in Table 2 were derived as follows: Five values of  $A_{graph}$  and  $A_{paint}$  were measured from adjacent areas of the sample, and for each pair, a contrast value was calculated, using equation (54). The average value of the five measurements is considered to be the final value of the contrast.

**Table 2: Thicknesses and contrasts of the Chromium samples**

Sample thickness ( $\mu\text{m}$ )	Contrast (PAI)	Contrast (IR)
193	$0.83 \pm 0.03$	$0.22 \pm 0.05$
220	$0.77 \pm 0.01$	$0.152 \pm 0.003$
229	$0.64 \pm 0.05$	$0.13 \pm 0.01$
247	$0.59 \pm 0.04$	$0.10 \pm 0.02$
257	$0.52 \pm 0.07$	$0.094 \pm 0.009$



Figures 30-31: Profiles of the chromium samples. The numbers at the titles of the graphs correspond to the numbers written on the samples shown in Figure 28 (a, e).



Figures 32-33: Profiles of the chromium samples. The numbers at the titles of the graphs correspond to the numbers written on the samples shown in Figure 28 (l, m).

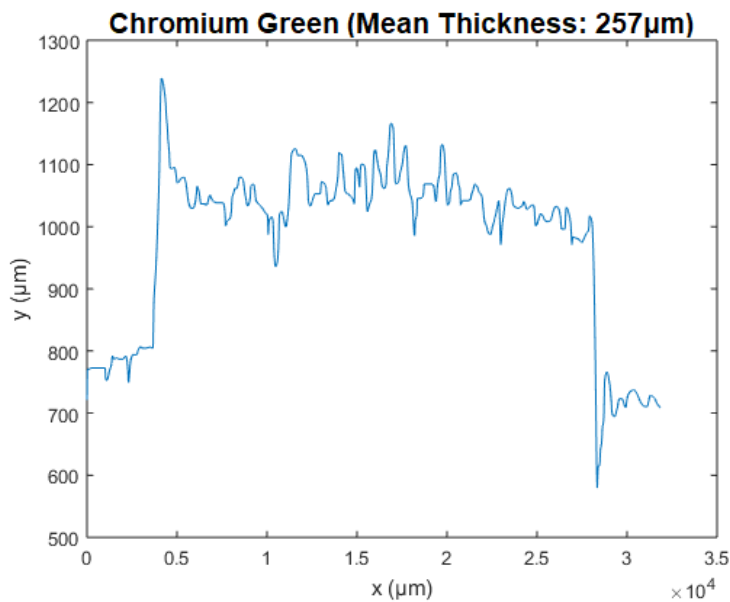


Figure 34: Profile of chromium sample 4. The number at the title of the graph correspond to the number written on the sample shown in Figure 28 (q).

Generally, light absorption in a medium follows the Beer-Lambert law, meaning that the intensity of the light ( $I$ ) at depth  $z$ , is  $I(z) = I_0 e^{-\mu z}$  (56), where  $I_0$ : the initial value of the intensity (at  $z=0$ ) and  $\mu$ : the absorbance coefficient of the medium. The contrast of an image is proportional to the light that manages to reach the absorber. Therefore, with the use of the values in Table 2, graphs of contrast-thickness were made. For both methods, the fitting model was  $y = az + b$  (57), because the exponential decrease in  $I(z)$  for a narrow domain near  $z=0$ , can be approximated by a linear function, due to Taylor's theorem.

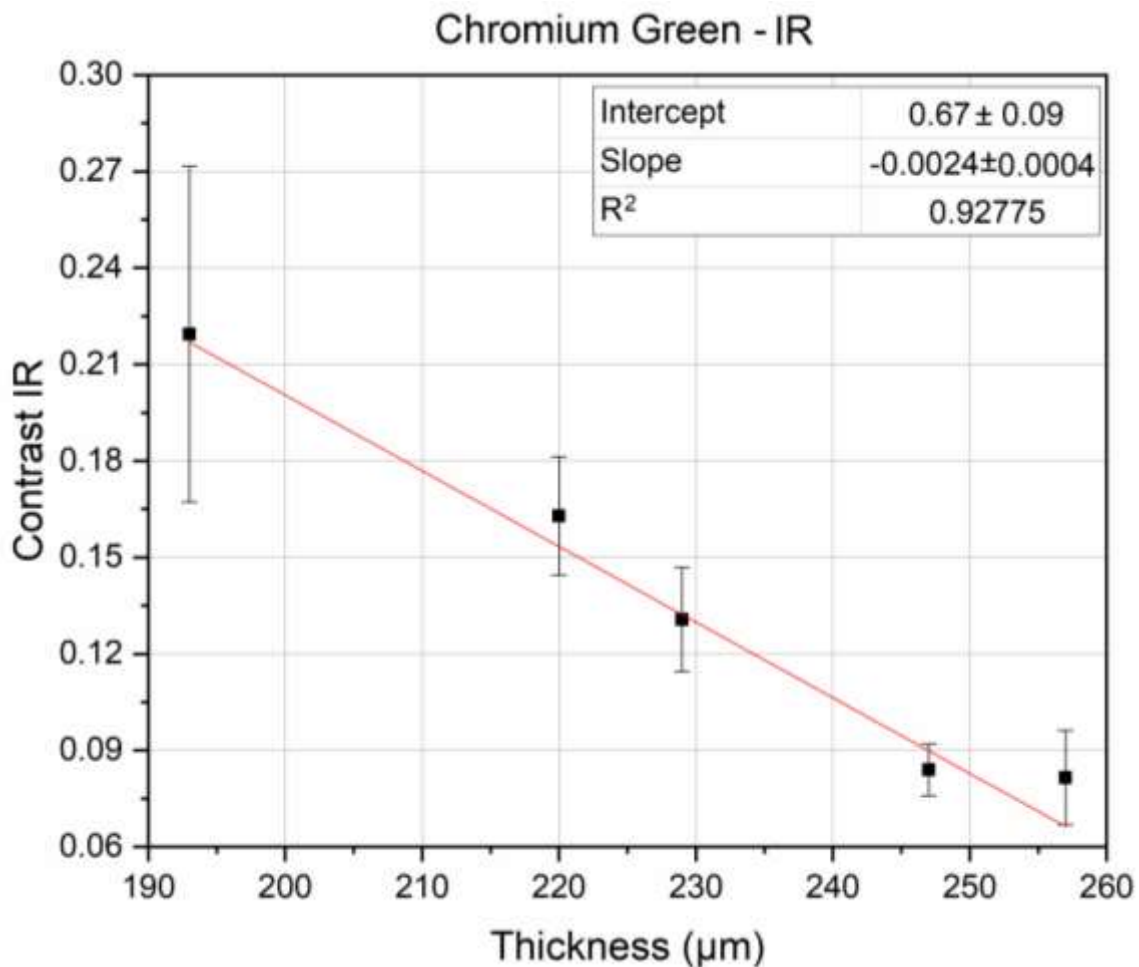


Figure 35: Linear fit of the contrast for the IR.

### Chromium Green - PA

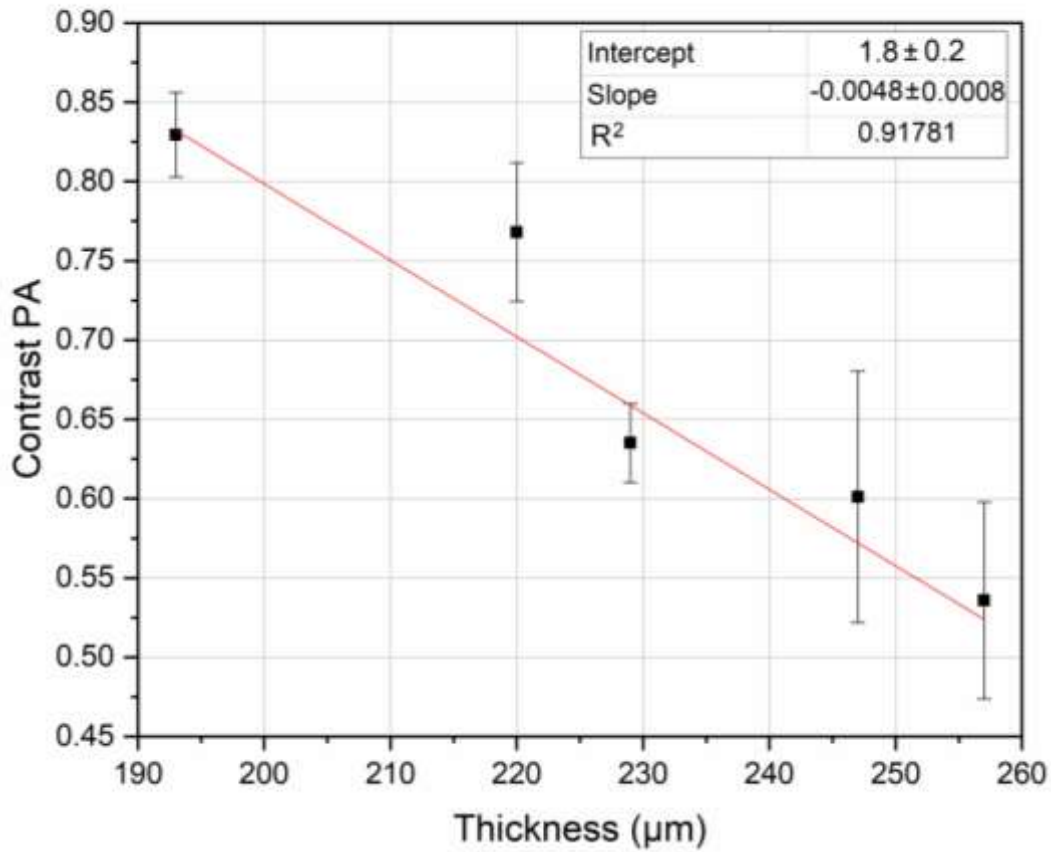


Figure 36: Linear fit of the contrast for the PAI.

### Comparison of imaging techniques

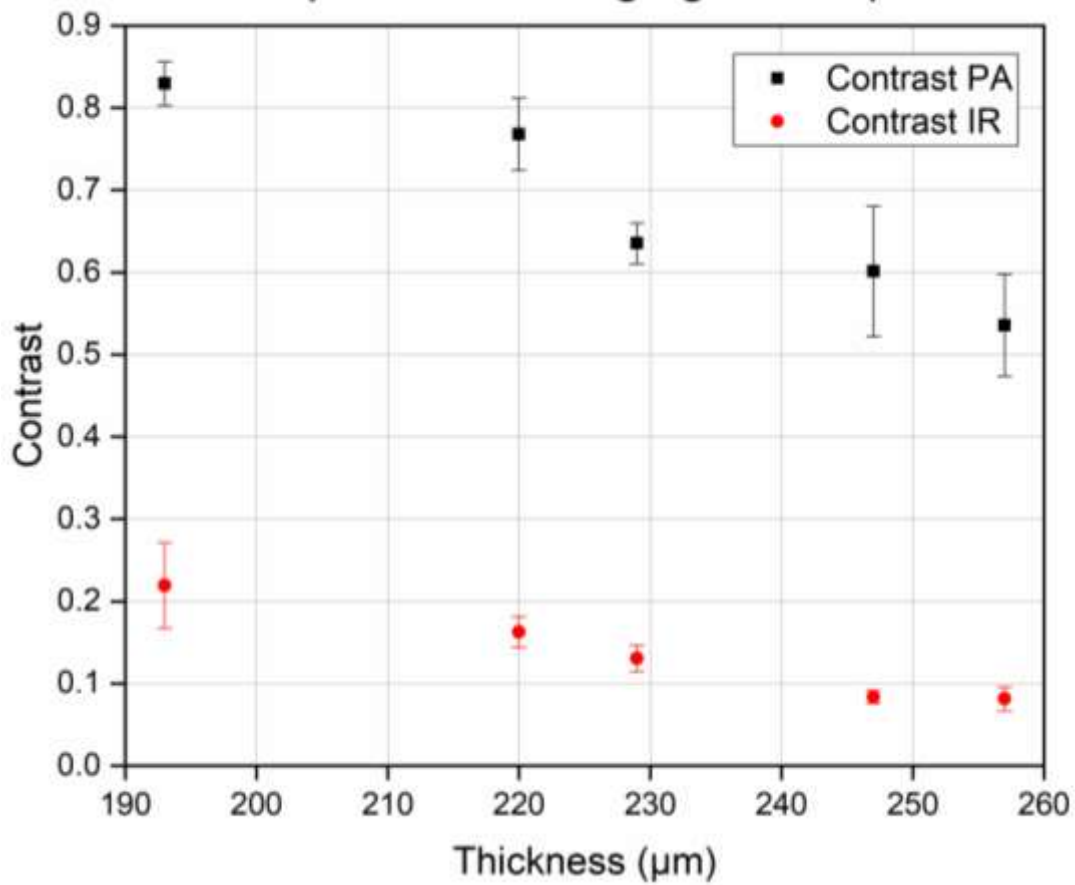


Figure 37: Aggregate graph of the two imaging methods.

In Figure 37, where the two methods are compared directly, it is clear that the PAI has an impressively larger contrast than the IR. As a matter of fact, the ratio  $\frac{C_{PA}}{C_{IR}}$  is near 5. In the case of the PAI, the light passes through the paint layer only once, thus the amount of light that reaches the underdrawings is larger. This is a possible reason why the values are so different.

## 5.2. Various pigments

In this section, the rest of the samples are presented. The image processing, as well as the calculation of the contrast for each sample, was done using the same methods that were described in 5.1.1. Because of the morphology of some samples, it was not possible to measure their thickness with the conventional profilometer that was available. This happened in cases where the entire surface was covered with the paint layer, and a zero-level for the thickness could not be considered. The profiles of the samples that could be measured are presented in Figures 38-47. In every figure, the first image is a brightfield view of the final sample, the second a brightfield view of the underdrawing of the sample before the application of the paint layer, the third the recovered pattern of the initial underlying sketch with the use of PAI and the fourth, the image that was acquired with IR. In both cases (PAI and IR), the processed image is presented.



Figure 38: Sample with paint layer consisted of Titanium white.

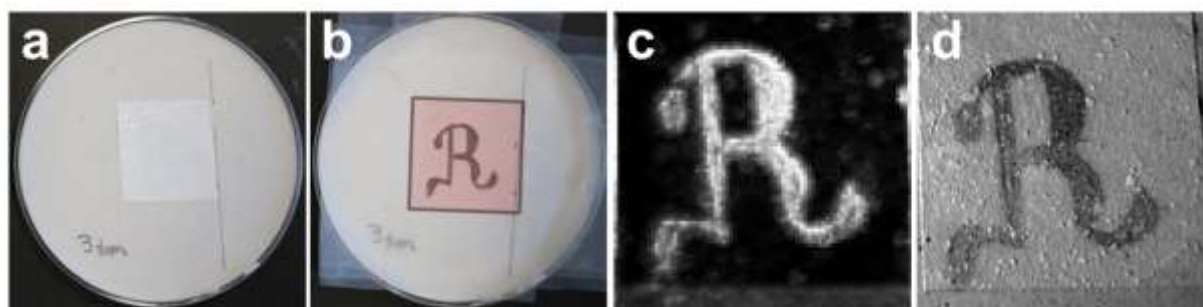


Figure 39: Sample with paint layer consisted of Titanium white.

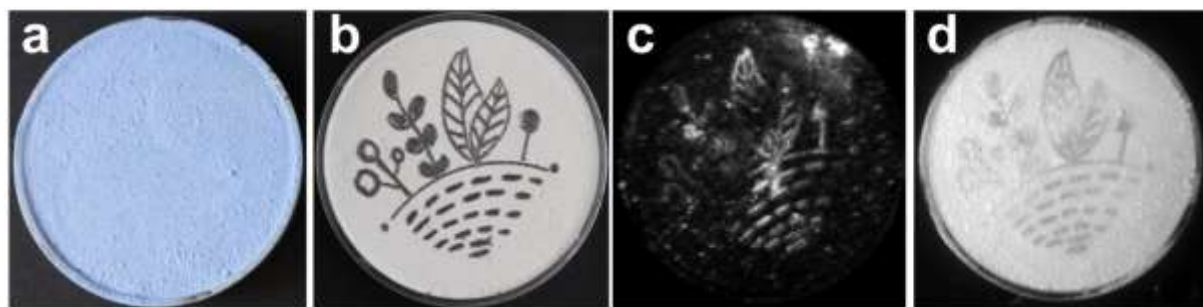


Figure 40: Sample with paint layer composed by Ultramarine Blue, Titanium White and Gypsum.

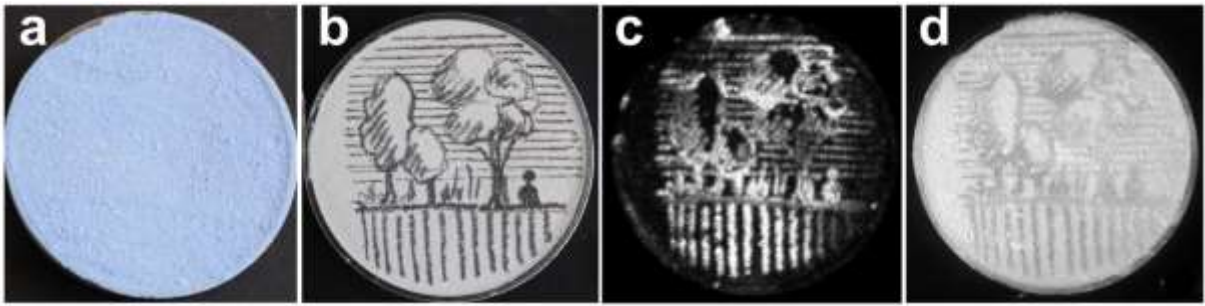


Figure 41: Sample with paint layer composed by Ultramarine Blue, Titanium White and Gypsum.

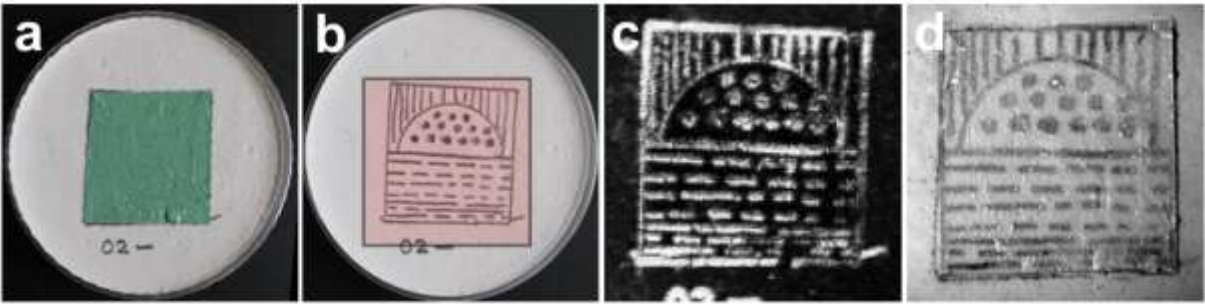


Figure 42: Sample with paint layer composed by Chromium Green and Titanium White.

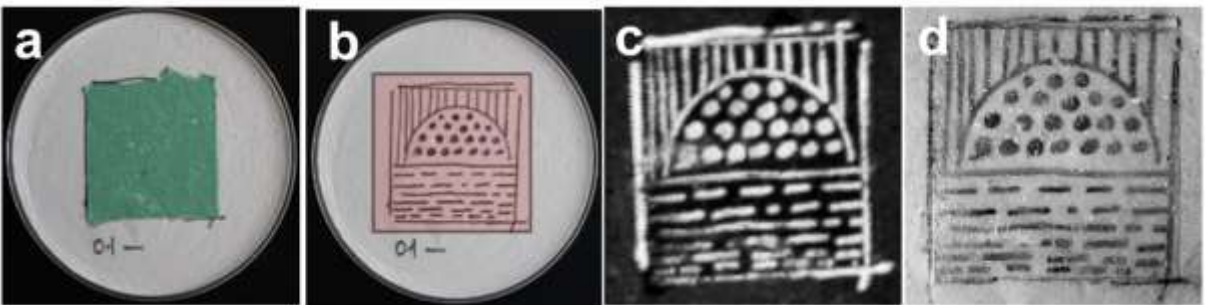


Figure 43: Sample with paint layer composed by Chromium Green and Titanium White.

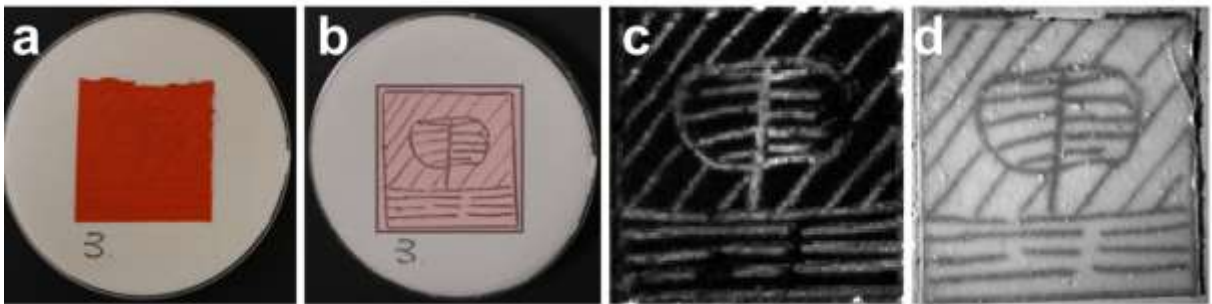


Figure 44: Sample with paint layer consisted of Minium.

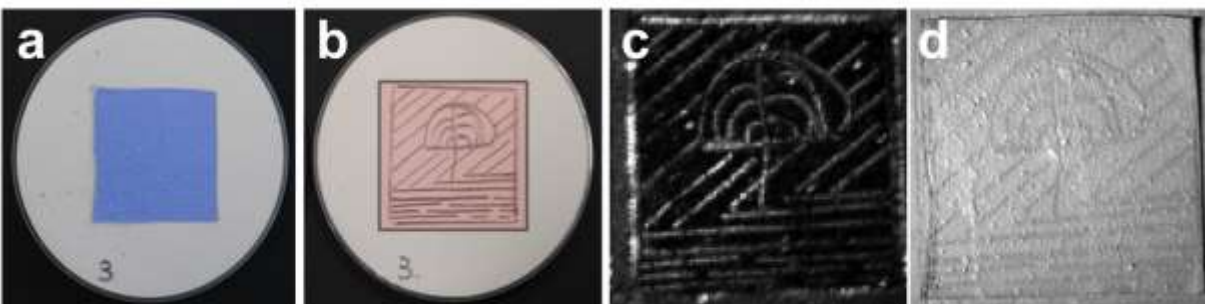


Figure 45: Sample with paint layer composed by Ultramarine Blue and Titanium White.

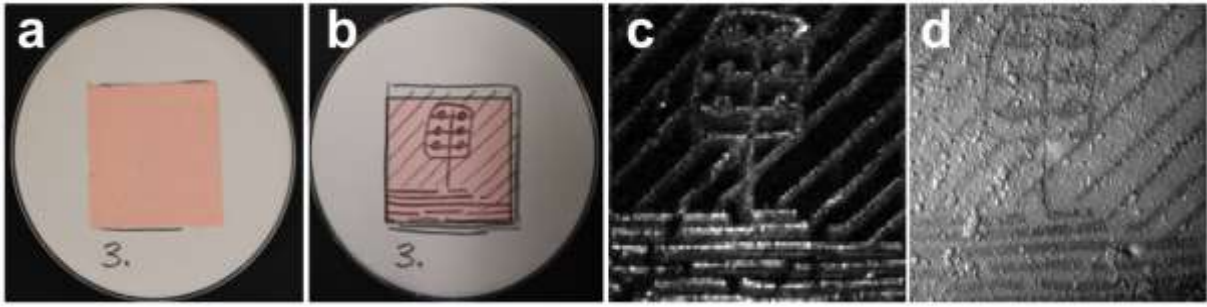


Figure 46: Sample with paint layer composed by Minium and Titanium White.

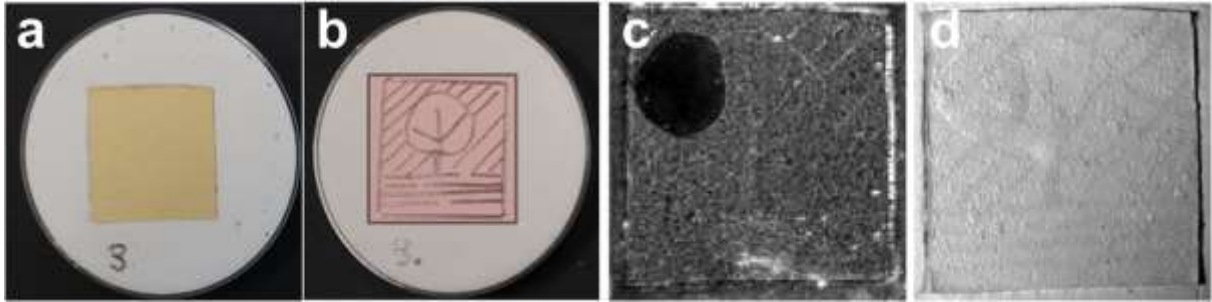
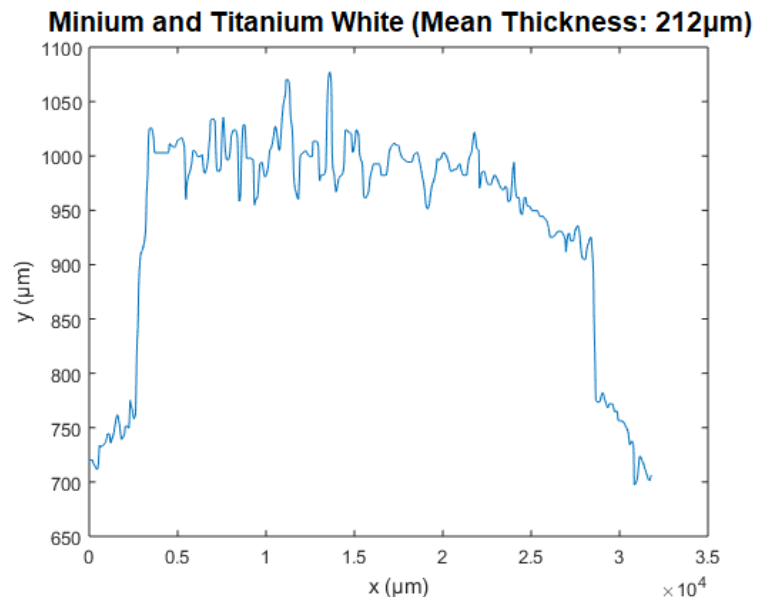
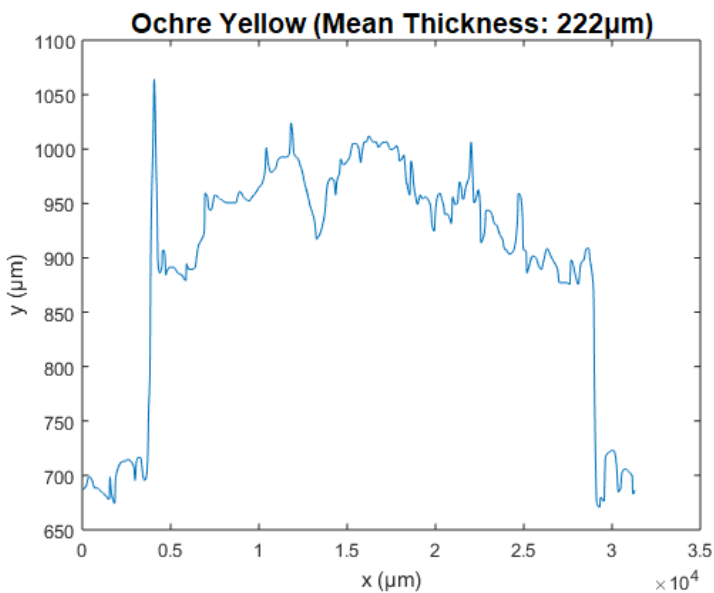


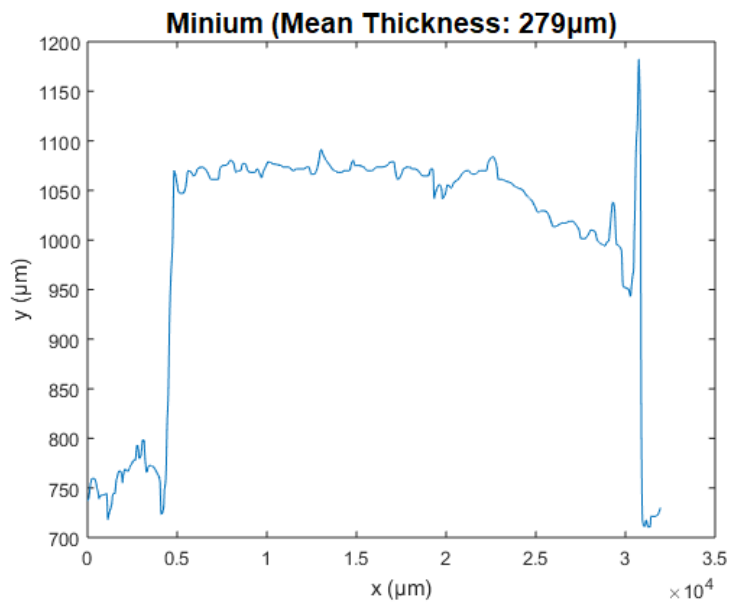
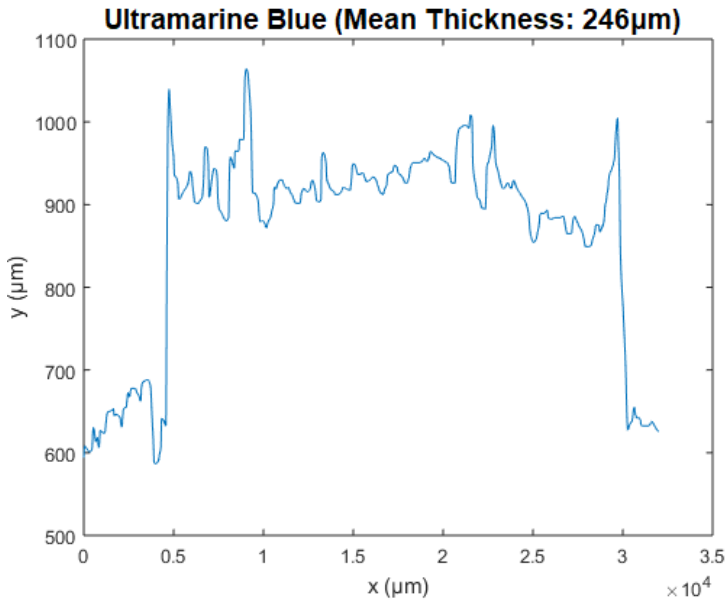
Figure 47: Sample with paint layer composed by Ochra Yellow and Titanium White.

From the images presented above, one can observe that the IR may provide much higher resolution but, even after the image processing, the contrast of the images is noticeably lower than the one obtained with the PAI. Furthermore, the anomalies into the volume of the paint layer (e.i. the gypsum lumps) and the small cavities that exist on the surface of the gypsum substrate seem to affect significantly the final image.

A very interesting conclusion can be deduced from the PAI of the sample presented in Figure 46c. A round area with very low signal is formed on the top left corner, preventing us from seeing the underlying sketch. This is the result of air existing between the gypsum substrate and the paint layer, which causes the ultrasound to decline abruptly. The reason of this rapid decrease is the wide difference of the values of the specific acoustic impedance ( $Z$ ). For acrylics,  $Z_{acr} = 2.86MRayl$  while for air,  $Z_{air} = 0.0004MRayl$ . Thus, without taking into consideration the loss of energy while the acoustic wave is traveling through a medium, from (9) is derived that after the interface between the paint layer and the air,  $T.E. = 1 - 0.9994^2 = 5.6 \cdot 10^{-4}$ .



Figures 48, 49: Profiles of the Ochra Yellow and Minium-Titanium White samples.



Figures 50, 51: Profiles of the Ultramarine Blue and Minium samples.

This means that approximately 0.6% of the initial energy manages to pass the interface, and this amount is not detectable by the transducer. This may be a problem for the image production but can be used in the framework of a restoration project that aims to locate detachments between the paint layers and the substrate, or cracks of the pigment.

**Table 3: Contrasts and thicknesses of the samples**

Figure number	Contrast (PAI)	Contrast (IR)	Contrast Ratio (PAI/IR)	Sample thickness (μm)
38	0.91	0.25	3.6	—
39	0.94	0.27	3.5	—
40	0.71	0.08	8.9	—
41	0.76	0.14	5.4	—
42	0.89	0.36	2.5	—
43	0.90	0.64	1.4	—
44	0.80	0.21	3.8	279
45	0.89	0.13	6.8	246
46	0.91	0.30	3.0	212
47	0.11	0.04	2.8	222

From the results presented in Table 3, it is once again made clear that the PAI produces images with higher contrast values compared to the ones acquired with IR.

It is also important to mention the fact that the transducer used for the needs of the experiment has a central frequency of 73MHz and its cutoff frequencies are  $f_{\min} = 30.7\text{MHz}$  and  $f_{\max} = 115.3\text{MHz}$ , as seen in Figure 52, and they correspond to -6dB, thus to a spectral amplitude equal to half its peak value. By convention we consider that the transducer is more sensitive to the frequencies that lie between this range (and specifically these that are near the center). Frequencies out of that region can be detected, but their amplitude is lower. This affects the efficiency of the acquired measurements, whose frequencies are approximately 6MHz [Fig. 53] and as a result, the image does not have the optimum contrast.

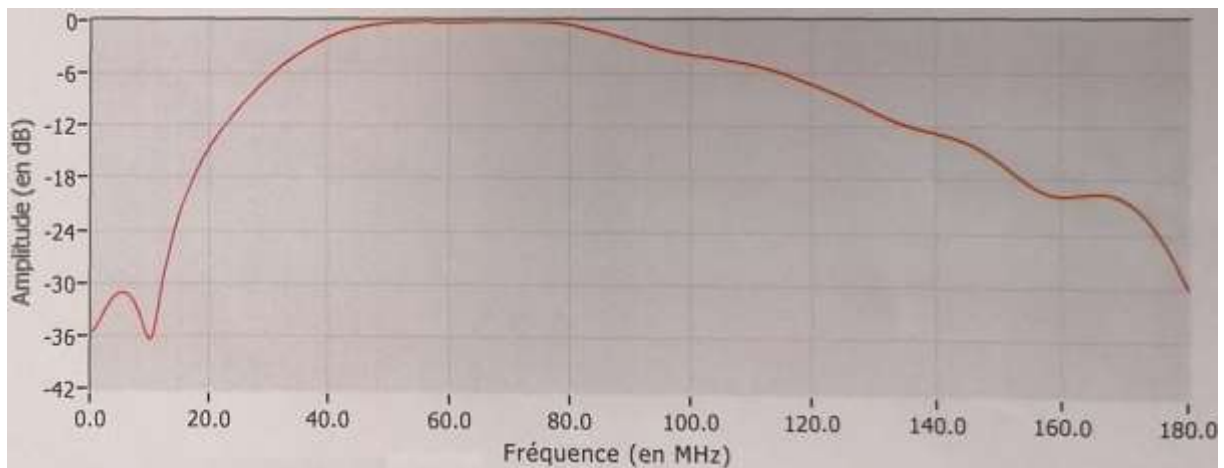


Figure 52: The bandwidth of the ultrasonic transducer used during the experiment. The horizontal axis represents the frequencies in MHz and the vertical the amplitude of the produced ultrasound, measured in dB.

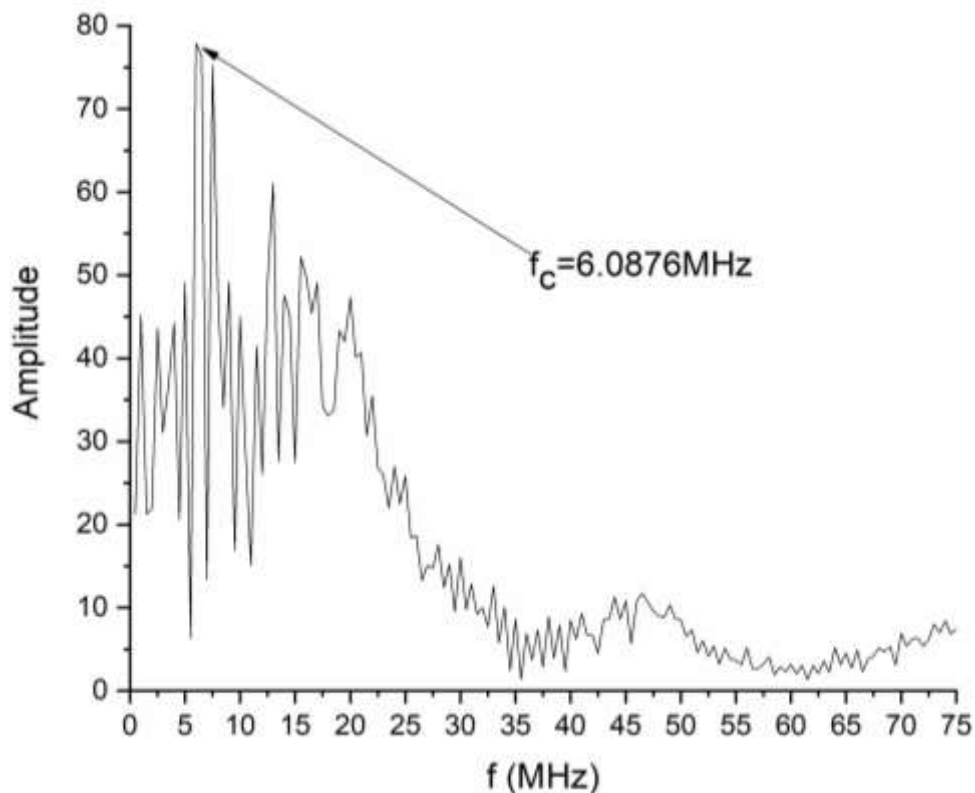


Figure 53: FFT of a typical PA signal acquired with the transducer used for this experiment due to illumination of graphite. The central frequency is  $f_c=6.0876\text{MHz}$ .

## 6. Discussion

The PA phenomenon has found its place in cultural heritage conservation over the last years. It is apparent that it can prevail over other imaging techniques that face limitations due to lacking illumination. In the case of PAI, even if a small amount of light manages to reach the absorber (in our case, the graphite or the material used to create the underdrawing), the ultrasound that is produced manages to traverse the distance between the absorber and the transducer without significant attenuation, and provide us with the information we need. On the contrary, in the existing optical techniques, the amount of light that reaches the area of interest has to travel again through the

sample in order to transfer the information, and that causes the intensity of the light that finally reaches the photodetector to decrease significantly, because its intensity decreases exponentially, as it has been previously mentioned (Beer-Lambert's law).

There are, nevertheless some drawbacks and disadvantages to the technique. To begin with, the acquisition of the PA waves is presently accomplished with the use of a water-immersion transducer. This excludes the description of the method as "non-contact", and may discourage some preservers from deciding to use it on artworks of great cultural significance. What is more, the use of a water-immersion transducer creates an additional, practical issue, which is the submergence of a mural into the water. There are, though, purpose-built ultrasonic gels that have the same refractive index -and optical properties- with water and thus, they could replace it in order to facilitate the measurements done on vertical surfaces. Nevertheless, the most important step towards the enhancement of the method is the use of air-coupled transducers, as non-contact methods in cultural heritage diagnostics is a huge prerogative. What is more, the time needed for the scanning of a relatively small surface ( $\sim 10\text{cm}^2$ ) with the aforementioned experimental apparatus, lasts approximately 2.5hrs. The aim of the project is to locate and reconstruct underdrawings of murals, which means that the scanning will have to cover a surface with a relative size of a few  $\text{m}^2$ . Thus, an augmentation of the speed of the motorized stages is necessary to take place. A step towards the augmentation of the speed is the use of a laser with shorter pulse duration, as well as a modification of the script that moves the XY stages in order to move continuously and not step by step. Another approach could be the use of galvo-mirrors that scan the specimen more rapidly. What is more, a limitation of the current set-up is the fact that the scanned area cannot exceed  $56.25\text{cm}^2$  because it was primarily made for other applications.

On the other hand, there are many potential enhancements that can occur in order to obtain more information after the scanning of a sample. To begin with, supplementarily to the detection of the ultrasounds due to the PA effect, with the use of the pulse-echo function of an ultrasonic transducer, which is based on the inverse piezoelectric effect, we could collect information about the morphology of the surface of the scanned area as well. The inverse piezoelectric effect occurs when a wave pressure is created due to the influence of an electric field over a piezoelectric crystal. This wave pressure reaches the upper surface of the sample and after its reflection it can be detected by the transducer. What is more, in order to achieve greater penetration of the incident light into the mural, wavefront shaping techniques could replace the simple, focused irradiation of the specimens, appropriately preparing the incident light for the interaction with the surface of the sample. Furthermore, a multispectral PA excitation approach combined with suitable spectral unmixing algorithms could enable a high sensitivity differentiation of absorbers presenting comparable absorption. Multispectral PA excitation means that the light source used for the excitation of the absorber has a number of different wavelengths, in order to be capable of producing signals from absorbers with different chemical composition, which absorb radiation at different wavelengths. In the same direction, an analysis in the frequency domain could provide additional information compared to the time domain. Last but not least, the use of a transducer designed to detect lower frequencies (for example with a spectrum that has the main frequency near 10MHz) could also enhance the efficiency of the experimental apparatus, as with the current instrument an important percentage of the produced PA signal is not being detected.

## 7. Summary

During the elaboration of the current study, the development of an innovative, non-destructive, detection technique for mural underdrawings was presented, based on the principles of PA microscopy. The method is based on the absorption of IR radiation by the material used for the underdrawing, which leads to the creation of a wave pressure that results in the creation of an ultrasonic wave, which is detected by the transducer. The raw signal is filtered and saved in a computer with a view to the creation of an image. It is important to mention the fact that the current work is a proof of concept study, as the mock-ups used during the measurements represent ideal cases of mural samples. Their substrate is very homogeneous and the sketches are drawn with graphite pencil, which is known from previous studies to have better absorbing traits at 1064 nm in comparison to carbon, which is the main material used for the underdrawings of murals. Better absorption leads to the production of ultrasound waves with higher amplitudes, which is translated as greater contrast in the constructed image. Nevertheless, the results of the experiment are very promising and the method has demonstrated the excellent capabilities of PAI to uncover hidden content in a mural sample consisting of different pigments, or even, gypsum. Lastly, we should report the fact that the specific technique is relatively low-cost and it does not require a very sophisticated or complex configuration. We hope that with proper modifications and enhancements, this experimental set-up could become a useful tool for art conservators and restorers.

## 8. References

- [1] Tserevelakis, G. J., Vrouvaki, I., Siozos, P., Melessanaki, K., Hatzigiannakis, K., Fotakis, C., & Zacharakis, G. (2017). *Photoacoustic imaging reveals hidden underdrawings in paintings*. *Scientific Reports*, 7(1). doi:10.1038/s41598-017-00873-7
- [2] Tserevelakis, G. J., Dal Fovo, A., Melessanaki, K., Fontana, R., & Zacharakis, G. (2018). *Photoacoustic signal attenuation analysis for the assessment of thin layers thickness in paintings*. *Journal of Applied Physics*, 123(12). doi:10.1063/1.5022749
- [3] Tserevelakis, G. J., Tsafas V., Melessanaki, K., Zacharakis, G. & Filippidis, G. (2019). Combined multiphoton fluorescence microscopy and photoacoustic imaging for stratigraphic analysis of paintings. *Optics Letters*, 44(5). <https://doi.org/10.1364/OL.44.001154>
- [4] Tserevelakis, G. J., Siozos, P., Papanikolaou, A., Melessanaki, K., & Zacharakis, G. (2019). *Non-invasive photoacoustic detection of hidden underdrawings in paintings using air-coupled transducers*. *Ultrasonics*. doi:10.1016/j.ultras.2019.06.008
- [5] Tserevelakis, G. J., Tsagkaraki, M., Siozos, P., & Zacharakis, G. (2018). *Uncovering the hidden content of layered documents by means of photoacoustic imaging*. *Strain*, e12289. doi:10.1111/str.12289
- [6] Zhang, Yi, *Measuring Acoustic Attenuation of Polymer Materials Using Drop Ball Test* (2013). *Dissertations and Theses*. 151.
- [7] Wang, L. V., & Wu, H. (2007). *Biomedical optics principles and imaging*. Somerset, NJ, USA: Wiley.
- [8] Jackson, J. B., Mourou, M. R., Whitaker, J. F., Duling, I. N., Williamson, S. L., Menu, M., & Mourou, G. A. (2008). *Terahertz time-domain reflectometry applied to the investigation of hidden mural paintings*. *2008 Conference on Lasers and Electro-Optics*. doi:10.1109/cleo.2008.4551489
- [9] Heitzmann, R. (2006). *Band Limit and Appropriate Sampling in Microscopy*, Chapter 3, p. 29-36 in: *Cell Biology*
- [10] Turner, N., Patterson, C., MacLennan, D. and Trentelman, K.(2018). *Visualizing underdrawings in medieval manuscript illuminations with macro-X-ray fluorescence scanning*. *X-Ray Spectrometry*, 48(4), pp.251-261. <https://doi.org/10.1002/xrs.2956>
- [11] Gettens, R. J., & Stout, G. L. (1947). *Painting Materials: A Short Encyclopedia* (4<sup>th</sup> ed.). Dover Publications.
- [12] Yao, J., & Wang, L. V. (2013). *Photoacoustic microscopy*. *Laser & Photonics Reviews*, 7(5), 758–778. doi:10.1002/lpor.201200060
- [13] Azhari, H., 2010. *Basics of Biomedical Ultrasound for Engineers*. Wiley. Chapter 9, p. 195-196
- [14] Daniilia, S., Tsakalof, A., Bairachtari, K., & Chryssoulakis, Y. (2007). *The Byzantine wall paintings from the Protaton Church on Mount Athos, Greece: tradition and science*. *Journal of Archaeological Science*, 34(12), 1971–1984. doi:10.1016/j.jas.2007.01.016

- [15] Thompson, D. V. (1956). *The Materials and Techniques of Medieval Painting (Dover Art Instruction)*. Dover Publications.
- [16] Bendada, A., Sfarra, S., Ibarra-Castanedo, C., Akhloufi, M., Caumes, J. P., Pradere, C., Batsale, J. C., Maldague, X. (2015). *Subsurface imaging for panel paintings inspection: A comparative study of the ultraviolet, the visible, the infrared and the terahertz spectra*. *Opto-Electronics Review*, 23(1). doi:10.1515/oere-2015-0013
- [17] Van Asperen de Boer, J. (1975). An introduction to the scientific examination of paintings. *Nederlands Kunsthistorisch Jaarboek (NKJ) / Netherlands Yearbook for History of Art*, 26, 1-40. Retrieved April 1, 2021, from <http://www.jstor.org/stable/24705332>
- [18] Van Asperen de Boer, J. R. J. (1968). *Infrared Reflectography: a Method for the Examination of Paintings*. *Applied Optics*, 7(9), 1711. doi:10.1364/ao.7.001711
- [19] Βεληβασάκη, Μ., Διπλωματική εργασία, Ηράκλειο 2016
- [20] Βρουβάκη, Η., Διπλωματική εργασία, Ηράκλειο 2016
- [21] White, R. M. (1963). *Generation of Elastic Waves by Transient Surface Heating*. *Journal of Applied Physics*, 34(12), 3559–3567. doi:10.1063/1.1729258
- [22] Brienza, M. J., & DeMaria, A. J. (1967). *LASER-INDUCED MICROWAVE SOUND BY SURFACE HEATING*. *Applied Physics Letters*, 11(2), 44–46. doi:10.1063/1.1755021
- [23] Von Gutfeld, R. J., & Melcher, R. L. (1977). *20-MHz acoustic waves from pulsed thermoelastic expansions of constrained surfaces*. *Applied Physics Letters*, 30(6), 257–259. doi:10.1063/1.89375
- [24] Wickramasinghe, H. K., Bray, R. C., Jipson, V., Quate, C. F., & Salcedo, J. R. (1978). *Photoacoustics on a microscopic scale*. *Applied Physics Letters*, 33(11), 923–925. doi:10.1063/1.90219
- [25] Fukunaga, K., Picollo, M. (2010). *Terahertz spectroscopy applied to the analysis of artists' materials*. *Applied Physics A*, 100(3), 591–597. <https://doi.org/10.1007/s00339-010-5643-y>
- [26] Adam, A. J. L., Planken, P. C. M., Meloni, S., & Dik, J. (2009). *TeraHertz imaging of hidden paint layers on canvas*. *Optics Express*, 17(5), 3407. doi:10.1364/oe.17.003407
- [27] Filippidis, G., Massaouti, M., Selimis, A., Gualda, E. J., Manceau, J.-M., & Tzortzakis, S. (2011). *Nonlinear imaging and THz diagnostic tools in the service of Cultural Heritage*. *Applied Physics A*, 106(2), 257–263. doi:10.1007/s00339-011-6691-7
- [28] Faries, M., Defoer, H. "Jan van Scorel's *Crucifixion* for the Oude Kerk, Amsterdam: The "finest painting in all of the regions of Flanders", " *Journal of Historians of Netherlandish Art* 12:2 DOI: 10.5092/jhna.2020.12.2.1
- [28] Filedt Kok, J. P. (1978). *Underdrawing and other technical aspects in the paintings of Lucas van Leyden*. *Netherlands Yearbook for History of Art / Nederlands Kunsthistorisch Jaarboek*, 29(1), 1–184. doi:10.1163/22145966-90000496

- [29] Syson, L., & Billinge, R. (2005). *Leonardo da Vinci's Use of Underdrawing in the 'Virgin of the Rocks' in the National Gallery and 'St. Jerome' in the Vatican. The Burlington Magazine, 147(1228), 450-463.*
- [30] Liang, H. (2011). *Advances in multispectral and hyperspectral imaging for archaeology and art conservation. Applied Physics A, 106(2), 309–323.* doi:10.1007/s00339-011-6689-1
- [31] Dik, J., Janssens, K., Van Der Snickt, G., van der Loeff, L., Rickers, K., & Cotte, M. (2008). *Visualization of a Lost Painting by Vincent van Gogh Using Synchrotron Radiation Based X-ray Fluorescence Elemental Mapping. Analytical Chemistry, 80(16), 6436–6442.* doi:10.1021/ac800965g
- [32] Adler, D. C., Stenger, J., Gorczynska, I., Lie, H., Hensick, T., Spronk, R., Wolohojian, S., Khandekar, N., Jiang, J. Y., Barry, S., Cable, A. E., Huber, R., Fujimoto, J. G. (2007). *Comparison of three-dimensional optical coherence tomography and high resolution photography for art conservation studies. Optics Express, 15(24), 15972.* doi:10.1364/oe.15.015972
- [33] Faries, M., *Underdrawings in the workshop production of Jan van Scorel – A study with infrared reflectography. Nederlands Kunsthistorisch Jaarboek (NKJ) / Netherlands Yearbook for History of Art, Vol. 26, Scientific examination of early Netherlandish Painting: Applications in art history (1975), pp. 89-228*
- [34] Hain, M.; Bartl, J.; Jacko, V. (2003). *MULTISPECTRAL ANALYSIS OF CULTURAL HERITAGE ARTEFACTS. Measurement of Physical Quantities, 3, 9-12*
- [35] Daukantas, P. (2018). *Cultural Artifacts in Terahertz Light. Optics and Photonics News, 29(3), 28.* doi:10.1364/opn.29.3.000028
- [36] Oshana, R. (2006). *Overview of Digital Signal Processing Algorithms. DSP Software Development Techniques for Embedded and Real-Time Systems, 59–121.* doi:10.1016/b978-075067759-2/50006-5
- [37] SILVERMAN, R. H., VINARSKY, E., WOODS, S. M., LIZZI, F. L., & COLEMAN, D. J. (1995). *THE EFFECT OF TRANSDUCER BANDWIDTH ON ULTRASONIC IMAGE CHARACTERISTICS. Retina, 15(1), 37–42.* doi:10.1097/00006982-199515010-00008